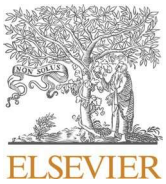
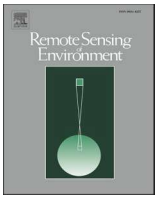
Remote Sensing of Environment 332 (2026) 115095



Contents lists available at ScienceDirect

Remote Sensing of Environment

journal homepage: www.elsevier.com/locate/rse





A deep learning-based framework for extracting spatial patterns of farmland shelterbelts in the three-north region of China using Sentinel-2 data

Hui Ma [a,b], Bingfang Wu [a,c,*], Fuyou Tian [a,*], Hang Zhao [a,b], Yifan Li [a,d], Mengxiao Li [a,b], Miao Zhang [a,b], Hantian Wu [e], Hongwei Zeng [a,b], Liang Zhu [a]

[a] State Key Laboratory of Remote Sensing and Digital Earth, Aerospace Information Research Institute, Chinese Academy of Sciences, Beijing 100101, China
[b] College of Resources and Environment, University of Chinese Academy of Sciences, Beijing 100049, China
[c] Beijing Yanshan Earth Critical Zone National Research Station, University of Chinese Academy of Sciences, Beijing 101408, China
[d] School of Computer Science, China University of Geosciences, Wuhan 430078, China
[e] Laboratory of Hydrogeological Survey, China Institute of Geo-Environmental Monitoring, Beijing 100081, China

ARTICLE INFO

Edited by Marie Weiss

Keywords:
Deep learning
Farmland shelterbelts
Landscape ecology
Sentinel-2
TNSFP
Windbreaks

ABSTRACT

As a dominant component of the Three-North Shelter Forest Program (TNSFP) in the Three-North Region of China (TNR), farmland shelterbelts (FSs or windbreaks) play crucial roles in reducing wind erosion and soil degradation. However, large-scale FS products are currently unavailable, posing challenges for their monitoring and optimization. To address this issue, we developed a deep learning-based framework to extract FSs from Sentinel-2 data and analyze their spatial patterns in the TNR. This study produced the first 10-m resolution FS map and the first vectorized FS network for the TNR in 2022. Our results indicated that the total length of FSs was 915.09 ± 21.45 thousand km, while the total area was 1575.18 ± 58.75 thousand ha. Both FS length and area were highest in Heilongjiang, Xinjiang, and Inner Mongolia, whereas the lowest values were observed in Beijing, Tianjin, and Qinghai. The average FS to farmland ratio, connectivity, and FS deviation angle were 2.83 % (± 0.11 %), 0.34, and 26°, respectively, highlighting potential for structural optimization. FSs were more concentrated, with well-structured spatial patterns in Northeast China and Xinjiang, while further construction efforts were needed in the Hetao Plain, Guanzhong Plain, and Hexi Corridor. The final FS map demonstrated robust performance across multiple evaluation metrics. Specifically, the pixel-based user's accuracy was 79.20 % and the producer's accuracy was 79.39 %. The average object-based F1-score was 84.13 % and the average length-weighted F1-score was 89.62 %. Overall, this study provides fundamental data and valuable insights to support agricultural infrastructure assessment and optimization.

1. Introduction

Farmland shelterbelts (FSs), which encompass trees planted on the perimeters of farmland, play critical roles in ensuring agricultural productivity and enhancing food security. They help stabilize the microclimate, reduce wind erosion, conserve soil moisture, and contribute to stabilizing crop yields (Cleugh, 2002; Grace, 1988; Kort, 1988; Li et al., 2020; McNaughton, 1988; Zhai et al., 2023; Zheng et al., 2016).

FSs are artificially cultivated and nonrenewable forests that need to be continuously cultivated, renewed, and managed to ensure their effectiveness. Therefore, monitoring and understanding FS distribution are essential for providing timely and adequate information for modern agricultural management.

Many large forest protection projects have been implemented worldwide, such as the Great Plains Shelterbelt Project in the USA (Orth, 2007), the Great Plan for the Transformation of Nature in the former Soviet Union (Brain, 2010), and the Three-North Shelter Forest Program (TNSFP) in China (Zhu and Zheng, 2019). The TNSFP has provided critical ecosystem services since 1978, with a total investment of CNY 93.3 billion (Zhai et al., 2023). The construction of FSs is an important part of the TNSFP. The overall plan of the TNSFP stipulates that all farmland in plains and oases should be covered by FS networks and that crop yields should increase by 10–15 %. According to the construction plans, FSs were planned to accounted for 9–12 % of the total planned

* Corresponding authors.
E-mail addresses: wubf@aircas.ac.cn (B. Wu), tianfy@aircas.ac.cn (F. Tian).

https://doi.org/10.1016/j.rse.2025.115095
Received 25 April 2025; Received in revised form 21 September 2025; Accepted 15 October 2025
Available online 23 October 2025
0034-4257/© 2025 Elsevier Inc. All rights are reserved, including those for text and data mining, AI training, and similar technologies.

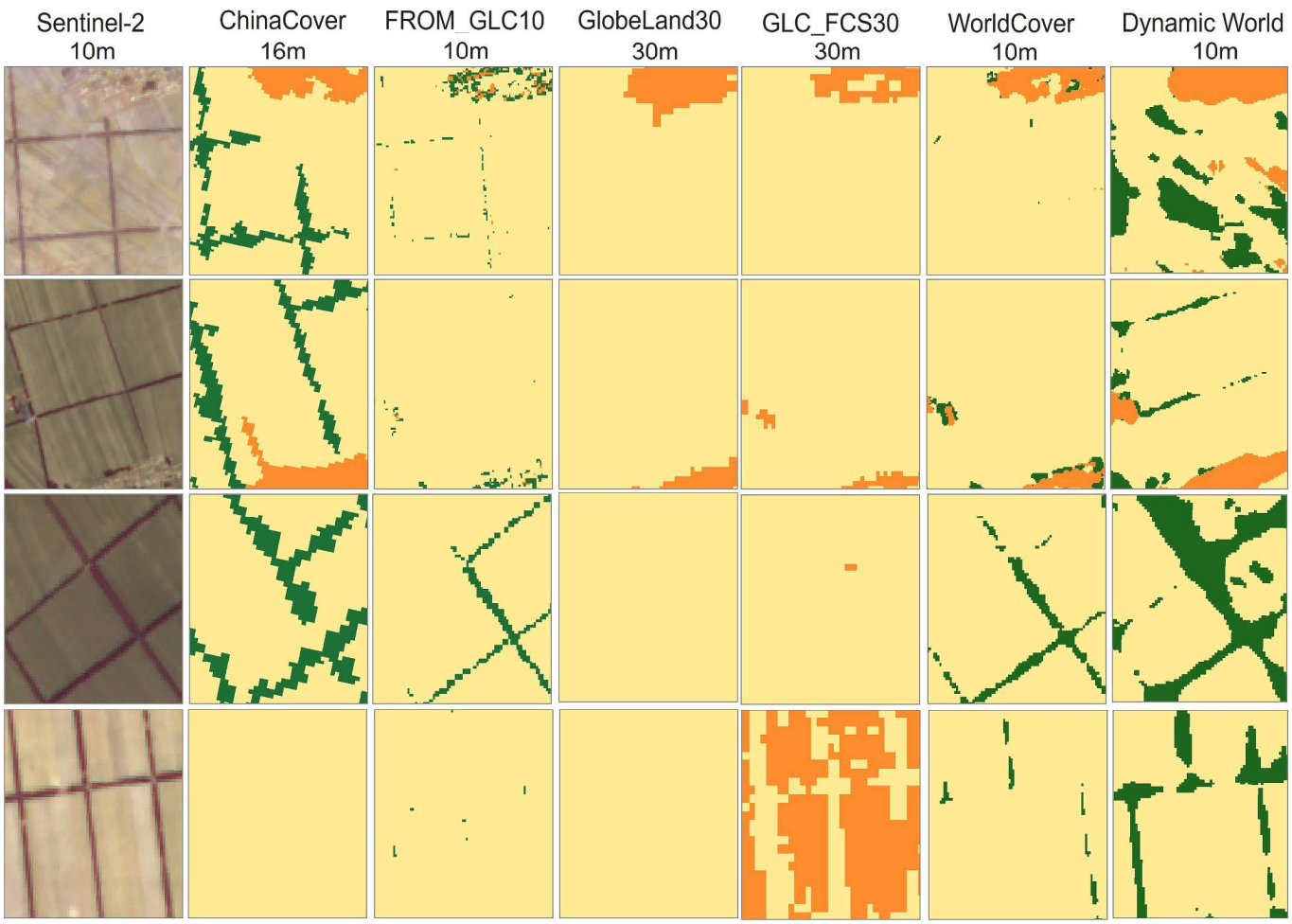


Fig. 1. Sentinel-2 images (false colour composite, with red representing FSs) and landcover datasets (yellow for farmland, green for tree cover, and orange for others). (For interpretation of the references to colour in this figure legend, the reader is referred to the web version of this article.)

protective forests, and by the fifth phase, FS networks were expected to protect more than 80 % of farmlands (National Forestry and Grassland Administration, 1978, 1986, 1996, 2001, 2011, 2019).

However, the FS distribution in the TNR remains insufficiently documented. Most existing land cover datasets, such as ChinaCover (Wu, 2017; Wu et al., 2024), FROM_GLC10 (Gong et al., 2019), GlobeLand30 (Chen et al., 2017), GLC_FCS30 (Zhang et al., 2021), WorldCover (Zanaga et al., 2022), and Dynamic World (Brown et al., 2022), do not clearly distinguish FSs (Fig. 1), which has left a gap in the monitoring of FSs.

Previous studies have explored the extraction of FSs using methods including visual interpretation and traditional machine learning algorithms, such as Random Forest (RF), Support Vector Machine (SVM), Maximum Likelihood Classification (MLC), and object-based approaches (Lei et al., 2020; Liu et al., 2018; Zhao et al., 2021; Zheng et al., 2013). However, most of these studies were conducted on a small scale, without large-scale testing or application. Manual visual interpretation requires substantial time and effort, making it impractical for large-scale applications. Traditional machine learning algorithms, which typically depend on shallow spectral features, are prone to confusion between FSs with surrounding farmland areas because of their spectral similarity (Tian et al., 2019). This classification ambiguity is further compounded by the heterogeneity of FS systems, as their species assemblages, structural configurations, and ecological functions vary substantially across landscapes (Liu et al., 2024; Yao et al., 2023). Deep learning methods, with their advanced feature extraction capabilities, have the potential to overcome these challenges by capturing deeper and more abstract features (Xu et al., 2022). Although deep learning has been widely applied in other fields of land cover classification (Li et al., 2022; Teixeira et al., 2023), its application in FS extraction remains relatively limited.

Therefore, this study developed a deep learning-based framework to extract FSs from Sentinel-2 data and analyze their spatial patterns in the TNR. The FSs mapped in this study include all tree belts within or around farmland areas, most of which are artificial shelterbelts, with a small portion potentially consisting of natural tree belts, such as the natural tree belts along riverbanks. Among the artificial shelterbelts, no distinction was made between farmland shelterbelts, roadside shelterbelts, and canal-side shelterbelts; instead, they were uniformly regarded as FSs, as they were constructed around farmland and provide a protective function. In addition, although some patch-shaped forested areas adjacent to farmland can also provide protective benefits, they are beyond the scope of this study. Here, we focus exclusively on tree belts within or around farmland areas, as they play a critical ecological role but remain underrepresented in existing land cover datasets.

Specifically, the objectives of this study are as follows:

1) Develop a deep learning-based framework to extract FSs from Sentinel-2 data.

2) Generate a vectorized FS network that integrates individual FS attributes with regional landscape metrics for comprehensive analysis.

3) Quantitatively characterize FS length, FS area, and FS spatial patterns within the TNR.

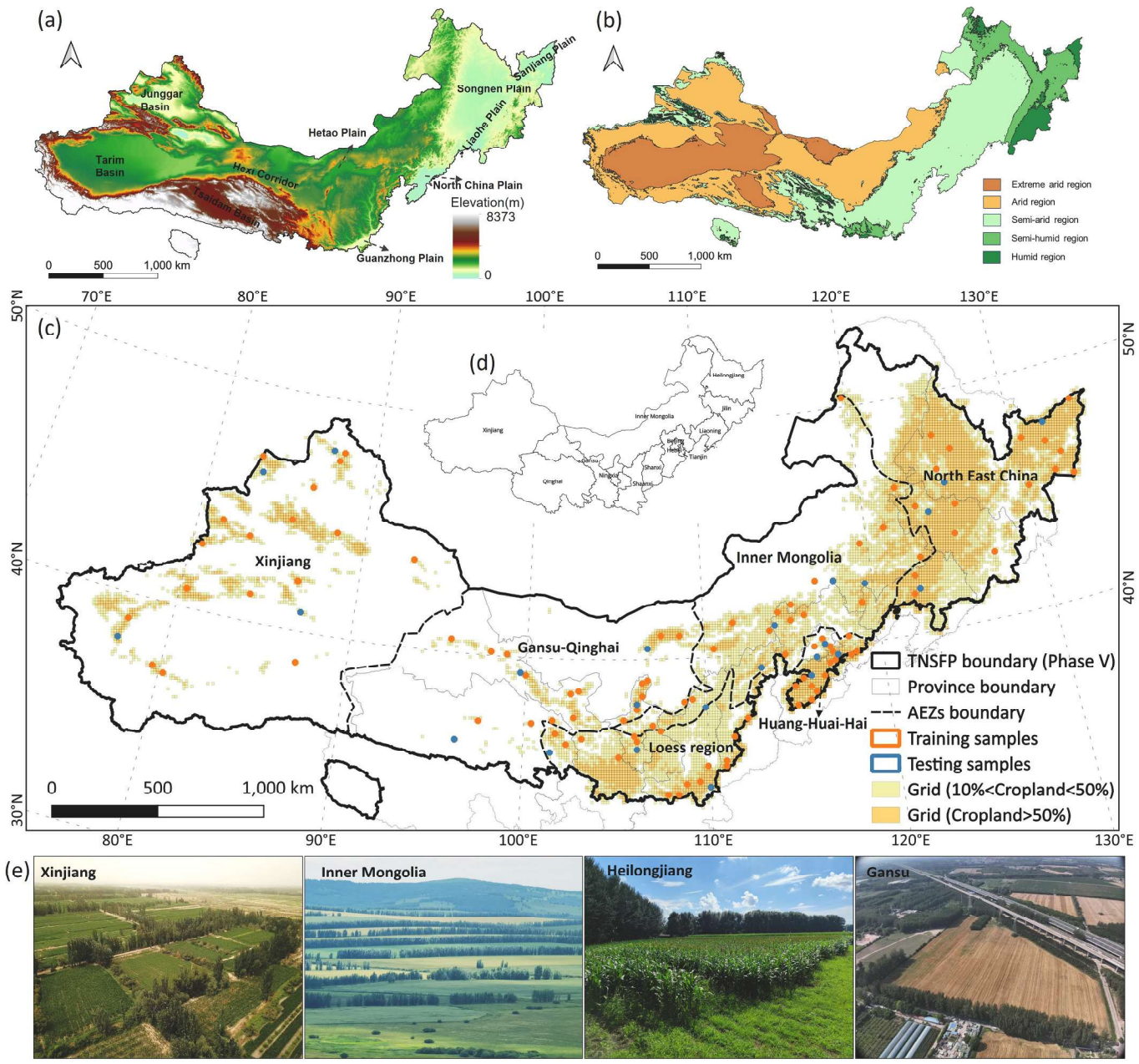


Fig. 2. (a) Elevation map. (b) Climate zone map. (c) Study area showing the Phase V construction scope of the TNSFP, farmland distribution, and sample locations (for model training and testing). (d) Provincial-level administrative regions of the TNR. (e) Field photos of the study area.

2. Study area and materials

2.1. Study area

The study area corresponds to the planned region of the fifth phase of the TNSFP, located in the TNR. This region is divided into Northwest China (Shaanxi, Gansu, Qinghai, Ningxia, Xinjiang, and western Inner Mongolia), North China (Beijing, Tianjin, Hebei, Shanxi, and central Inner Mongolia), and Northeast China (Heilongjiang, Jilin, Liaoning, and northeastern Inner Mongolia). In this region, which extends more than 4000 km from east to west, the heterogeneity of environmental conditions and vegetation is considerable (Zheng et al., 2016). The annual precipitation ranges from 400 mm (east) to 25 mm (west), and the moisture conditions vary from semi-humid (east) to semi-arid (middle) and arid (west) (Li et al., 2012).

The TNSFP has been implemented in this region and is planned to conclude in 2050, encompassing three stages (1978–2000, 2001–2020, and 2021–2050) and eight periods (1978–1985, 1986–1995, 1996–2000, 2001–2010, 2011–2020, 2021–2030, 2031–2040, and 2041–2050) across 725 counties and 13 provinces, covering an extensive area of 4.07×10^8 ha (42.40 % of China) (Fig. 2). The TNSFP is often referred to as China's "Green Great Wall" and is the world's largest afforestation project (Zhai et al., 2023). The program goals aims to enhance environmental conditions, such as preventing the erosion of mobile sand by wind and mitigating soil and water losses. Build systematic FSs in the TNR is an important means of achieving these goals (Zheng and Zhu, 2015a, 2015b). The FS construction areas designed in this project are distributed primarily across the Sanjiang Plain, Songnen Plain, Liaohe Plain, North China Plain, Guanzhong Plain, Hetao Plain, Hexi Corridor, and oasis regions of Xinjiang.

In this study, the entire study area was divided into zones due to variations in climate and phenology. We adopted the agroecological

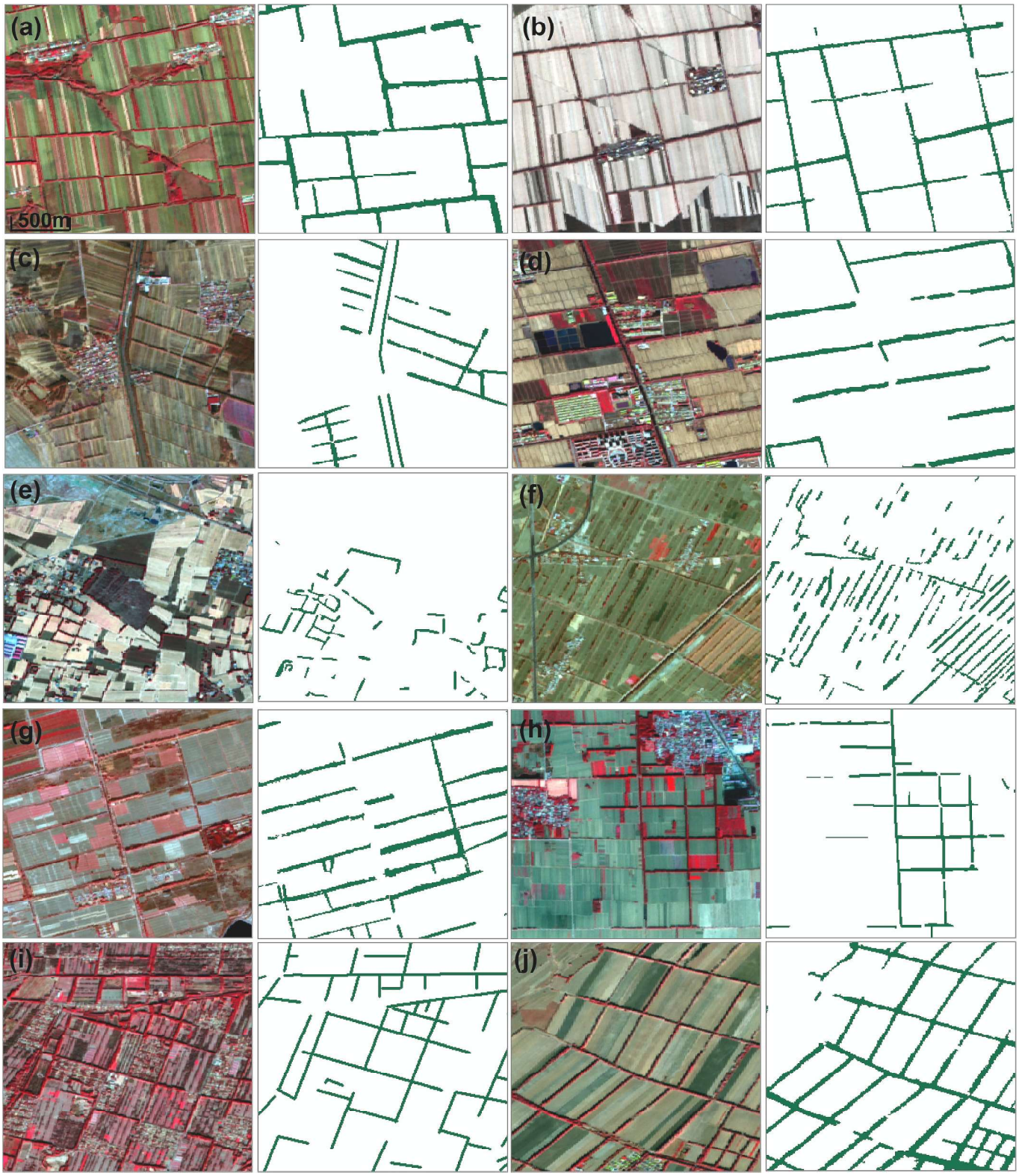


Fig. 3. Sentinel-2 images and labels of different FS landscapes: (a) Heilongjiang, (b) Jilin, (c) Liaoning, (d) Tianjin, (e) Inner Mongolia, (f) Ningxia, (g) Gansu, (h) Hebei, (i) Southern Xinjiang, and (j) Northern Xinjiang.

zones (AEZs) introduced by CropWatch (Gommes et al., 2015; Wu et al., 2015). The AEZs are divided based on crop type, agricultural production potential, and environmental conditions. We made several adjustments to better align the zoning with our study area, ensuring that each zone contained a sufficient distribution of FSs for analysis. Specifically, Xinjiang and Gansu were separated into distinct zones, while Gansu and Qinghai were merged into a single zone (Fig. 2).

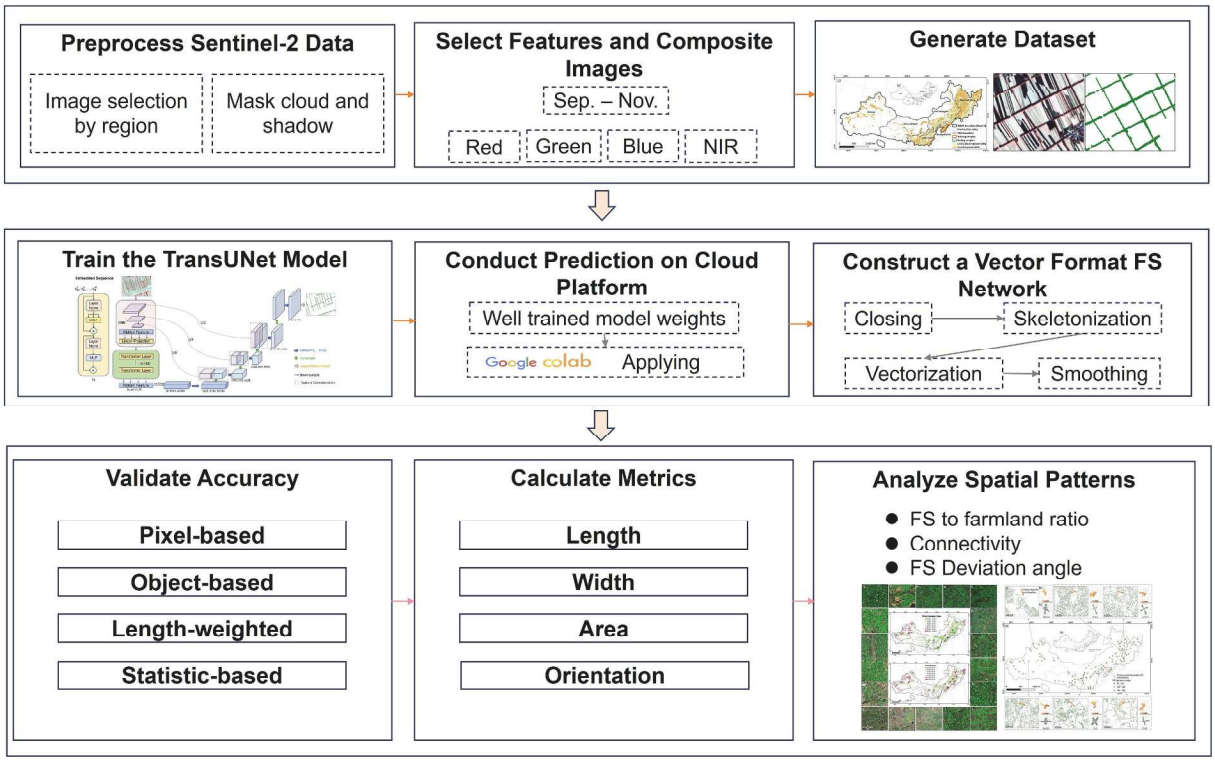


Fig. 4. Overall workflow of FS mapping.

2.2. Satellite data

Sentinel-2 Level-2A surface reflectance images (SR), which were accessed via the Google Earth Engine, were used in this study. These images were selected with cloud cover ranging from 0 % to 20 %, ensuring high-quality data for analysis. Bands 2 (blue), 3 (green), 4 (red), and 8 (near-infrared) were specifically utilized, with a spatial resolution of 10 m. The temporal scope of image acquisition was from September 1, 2022, to November 1, 2022. Images of the same location were combined via median-based image compositing.

2.3. Reference data

The reference data comprised two components: one part was used for model training and testing, and the other was reserved for independent validation of the produced FS map.

2.3.1. Training data for model

To obtain data for model training (and validation, testing), we adopted a stratified random sampling approach to ensure representativeness and spatial coverage. The study area was gridded into 12.5 km × 12.5 km grids, and only those with more than 10 % cropland coverage were retained to ensure adequate representation of target features (Fig. 2). We then performed a two-tier stratification: first, grids were grouped by agro-ecological zones (AEZs); second, within each AEZ, grids were further stratified based on cropland proportion (>50 % and 10–50 %). Equal numbers of samples were randomly drawn from each stratum to account for both ecological heterogeneity and landscape complexity (e.g., fragmented cropland landscapes tend to have higher land cover diversity and more scattered FS spatial patterns). In total, 120 grids were selected: 96 for training (yielding 18,808 image patches of 224 × 224 pixels) and 24 for testing, evenly distributed across all strata (Fig. 2). The sample dataset was constructed using two approaches: manual visual interpretation and manual refinement of results from previous studies (Fig. 3).

2.3.2. Validation data for map accuracy

Since we produced FS map in both raster and vector formats, we constructed separate validation datasets to independently evaluate the performance of each representation.

For the raster-format FS map, we followed the “good practice” recommendations (Olofsson et al., 2014) and used the stratified random sampling design to generate validation samples for accuracy assessment. Specifically, we divided the map into two strata: FS and non-FS. A total of 2100 pixels were sampled (minimum required: 927), including 1000 FS and 1100 non-FS pixels to ensure adequate representation given their imbalanced proportions in the map (Fig. A3). The sampled pixels were visually interpreted based on high-resolution imagery or UAV-based field observations.

For the vector-format FS map, the results were first gridded, and the grids were stratified into three equal-sized strata based on the total length of FSs within each grid, ranked from high to low. From each stratum, 70 grids of 2.5 km × 2.5 km were randomly selected, resulting in a total of 210 validation grids (Fig. A4). Vector reference labels were manually delineated for each grid.

2.3.3. Official statistics

Official statistics on FS area were collected from data released by relevant government authorities (Table A1). The official public data were limited to Heilongjiang, Jilin, Liaoning, Xinjiang, and Bayannur City in Inner Mongolia. Data for other regions are currently unavailable on official platforms.

2.4. Auxiliary data

The farmland data were derived from the “cropland” class of the ESA WorldCover dataset (Zanaga et al., 2022), to calculate the farmland area and define a coarse mask (dilated by 5 pixels) for constraining extraction area.

China’s daily meteorological observation dataset for this study was primarily sourced from the Resource and Environmental Science Data

Platform, which provides wind records from 163 meteorological stations within the study area for 2000–2020. Furthermore, for 63 of the stations, wind data for 2021 and 2022 were supplemented using publicly available records from the National Centers for Environmental Information (NCEI) website (Table A1).

High-resolution imagery from multiple sources was used to support sample labeling and shelterbelt width estimation, including GF-1 imagery (2 m spatial resolution) (Fig. A2), along with ESRI World Imagery and Google Earth imagery (Table A1).

The UAV imagery acquired at 10 sites across Northeast China (Fig. A3 and A5), covering a total area of 7.96 km^2, supported the validation of the FS map. The UAV imagery was acquired at an altitude of approximately 120 m using a nadir (vertical) camera orientation, with a horizontal positioning accuracy of 3 cm.

All relevant data and sources have been compiled in Table A1.

3. Method

FSs are distinguishable in remote sensing imagery because of their unique traits: they are distributed within or around farmlands, typically forming strip-like formations that interlace to create a grid-like pattern, and they exhibit spectral differences, which set them apart from the surrounding farmland. Utilizing these characteristics, we devised a mapping framework capable of automatically generating a detailed 10-m-resolution FS map in the TNR and obtaining a vector-based FS network with attributes, thereby facilitating in-depth analysis of the FS spatial patterns.

The framework is illustrated in Fig. 4. First, Sentinel-2 imagery was selected based on the study area and processed for cloud removal. Subsequently, median compositing was performed using imagery acquired between September 1 and November 1, resulting in a composite image containing four bands: red, green, blue, and near-infrared (NIR). Based on the composite imagery and high-resolution imagery, training and testing samples were generated. The samples were then used to train the TransUNet model (Chen et al., 2021). Prediction across the TNR was conducted on the Google Colab cloud platform, producing a raster format FS map. The raster FS results were post-processed through morphological closing, skeletonization, vectorization, and smoothing to generate the vectorized FS network. Accuracy assessments for the produced FS map were conducted from four perspectives—pixel-based, object-based, length-weighted and statistic-based—to evaluate both the FS raster and vector results. Finally, the length, width, area, and orientation of FSs were calculated. Based on these, three landscape indices—FS to farmland ratio, connectivity, and FS deviation angle—were derived to comprehensively assess the spatial patterns of FSs.

3.1. Model training and prediction

In this study, the TransUNet model (Chen et al., 2021) was adopted as the classifier because of its relatively high accuracy in remote sensing applications (Chen et al., 2024). ResNet-50 was adopted as the CNN backbone. The patch size in the transformer layers was set to 16 × 16 pixels for further projection into an embedded sequence. The Dice-Cross Entropy Loss function (0.5 CE + 0.5 Dice) was leveraged to train TransUNet. The batch size was set to 32 to fit into the GPU memory (NVIDIA Tesla V100-SXM2 32 GB), and the maximum number of training epochs was set to 300. TransUNet was trained with the SGD optimizer with a learning rate of 0.01, momentum of 0.9, and weight decay of 1e-4. It was implemented with the PyTorch package.

To minimize both the time and storage expenses associated with image transmission, we integrated an FS mapping framework within cloud-based platforms. This included the utilization of the Google Earth Engine (GEE), Google Drive, and Google Colab, as demonstrated by Carneiro et al. (2018). The initial steps of Sentinel-2 image preprocessing and the assembly of composite images were executed on the GEE platform. The composite images were subsequently archived on Google Drive for convenient access and management. The trained TransUNet model was deployed on the Colab platform to retrieve composited images from Google Drive, after which predictions for FSs were obtained.

3.2. Postprocessing

Because this study focused exclusively on FSs within or around farmland areas, we first applied a coarse farmland mask (introduced in section 2.4) to the predicted results, ensuring that only FSs located within coarse farmland extents were retained.

The predicted FS map was in raster format, whereas the vectorized FS network provides more information for further study. The study area was partitioned into 25 km × 25 km grids for vectorization and the calculation of FS ecological indicators. This grid size was chosen to reduce computational memory demands and to address scale effects: while smaller grids capture finer details, they may yield unstable estimates of landscape metrics at broader administrative levels, whereas larger grids risk smoothing out local information. As noted by Lv and Zhao (2023), scale effects in FS ecological indicators tend to diminish once the spatial extent exceeds 20 km, partially supporting the use of a 25 km grid. To obtain a vector-based FS network, several postprocessing steps were conducted on the FS map. First, morphological closing operations (with a kernel size of 3 pixels) were applied to the FS map to address small discontinuities that may form during segmentation, which could affect the quality of the vectorized results (Fig. A1). Next, skeletonization was performed using the widely used Zhang–Suen (*Z*-S) algorithm (Zhang and Suen, 1984) to extract the skeleton of each FS. The resulting skeletons were then vectorized into polylines to represent the linear geometry of the FS network. Finally, the Douglas–Peucker (DP) algorithm (Douglas and Peucker, 1973) was applied to smooth the vectorized polylines and reduce noise while preserving the overall structural integrity (Fig. A1).

3.3. Calculating FS indicators

To analyze the spatial pattern of FSs, we quantified their orientation (derived from the coordinates of the start and end points for each FS), length, width, and area, and subsequently calculated a series of landscape-level metrics based on these attributes.

The length of each FS was initially calculated using ArcPy's geometry analysis tools. Then, a regression-based correction was applied using the reference dataset to quantify and mitigate systematic biases in the extracted lengths.

FS width was estimated at the provincial level using simple random sampling, treating each province as an independent unit. Following Cochran's sampling theory (Cochran, 1977), the target was to achieve a margin of error of ±2 m for the average FS width at the 95 % confidence level. An initial survey with 20 random sites per province provided the sample standard deviation, which served as a proxy for the population standard deviation to determine the minimum required sample size. Additional samples were added iteratively until this precision requirement was met. In total, 764 points were collected (Fig. 8 and Table A2). Representative FS widths were manually measured from high-resolution imagery, and the sample mean was used as an unbiased estimator of provincial-level average FS width.

Given the resolution limitations, it is difficult to accurately calculate the area of FSs using pixel-counting-based methods (Muro et al., 2025; Zheng et al., 2013). In 10 m resolution imagery, mixed pixels significantly affect the extraction of narrow linear features like FSs, which are typically only 10–30 m wide (1–3 pixels). This leads to width distortion and introduces substantial bias in pixel-based area estimates, whereas length measurements are more robust (Muro et al., 2025). Therefore, we estimated FS area by multiplying the FS length by the FS width, following the method of Zheng et al. (2013, 2025), which better suits the

geometric characteristics of FSs—narrow linear features with relatively consistent width along their length. FS area was first calculated at the provincial level, after which the total FS area in the study area was derived, with uncertainty quantified using standard error propagation under the assumption of independence between FS length and FS width (95 % confidence interval) (Eqn 1, 2, 3 and 4).

$$A_i = bL_iW_i \tag{1}$$

$$A_{total} = \sum_{i=1}^{M} A_i \tag{2}$$

$$SE_{A,i} = \sqrt{W_i^2 SE_{L,i}^2 + L_i^2 SE_{W,i}^2} \tag{3}$$

$$SE_{A,total} = \sqrt{\sum_{i=1}^{M} \left(SE_{A,i}\right)^2} \tag{4}$$

Where L_i, W_i, A_i are the extracted FS length, estimated average FS width and FS area for the i th province; b is the regression coefficient obtained from a no-intercept linear regression between the extracted FS lengths and the corresponding reference lengths in samples; A_{total} is the total estimated FS area of the study area, $SE_{A,total}$ is the corresponding standard error; M is the total number of provinces considered; $SE_{L,i}$, $SE_{W,i}$, $SE_{A,i}$ denote the standard error of FS length estimation, FS width estimation and FS area estimation for the i th province.

The amount and configuration are the fundamental elements of landscape patterns (Riitters, 2019). The FS abundance was quantified on the basis of the FS to farmland ratio, and the spatial configuration and integrity of FS networks were assessed on the basis of the connectivity at the landscape scale (Forman, 1995; Li et al., 2003; Shi et al., 2011; Zhou and Sun, 1994); moreover, the rationality of FS orientation was assessed on the basis of the FS deviation angle. These indices were calculated as follows.

(a) FS to farmland ratio

FS to farmland ratio describes abundance on the basis of the characteristics of an area and the number of FS networks at the landscape scale. It is expressed as Eqn 5 (Li et al., 2003; Li et al., 2020; Shi et al., 2011; Zhou and Sun, 1994):

$$FS\ to\ farmland\ ratio = S_b/A \tag{5}$$

where S_b is the FS area and A is the area of farmland to be protected.

(b) Connectivity

Connectivity is an index that reflects network integrity and completeness. It is the ratio of the total number of existing connected FSs to the maximum number of possible connected FSs in the network. The connectivity of a FS network is expressed as Eqn 6, 7, 8, 9 and 10 (Forman, 1995; Li et al., 2003; Li et al., 2020; Shi et al., 2011; Zhou and Sun, 1994):

$$Connectivity = [N_b - (n-1)]/L_{max}(V) \tag{6}$$

$$L_{max}(V) = V - 1\ (\mathrm{V} = 2, 3) \tag{7}$$

$$L_{max}(V) = 3 \times (V-2)/2 + 1\ (\mathrm{V} = 4, 6, 8) \tag{8}$$

$$L_{max}(V) = 3 \times (V-3)/2 + 2\ (\mathrm{V} = 5, 7) \tag{9}$$

$$L_{max}(V) = 2 \times \left(int\sqrt{V}\right)^2 - 1 + 2 \times \left(V - \left(int\sqrt{V}\right)^2\right) - sgn\left(V - \left(int\sqrt{V}\right)^2\right)\ (\mathrm{V} > 8) \tag{10}$$

where N_b is the total number of FSs; n is the number of patches to be protected before the FSs are constructed; V is the number of nodes; and $L_{max}(V)$ is the maximum number of possible FSs.

(c) FS deviation angle

FS deviation angle, defined as the angle between the actual FS orientation and the ideal orientation (perpendicular to the dominant harmful wind direction), can influence the windbreak efficiency of FSs. The windbreak efficiency of FSs is typically expressed as the downwind distance over which a specified reduction in wind speed is achieved (Zhu, 2023; Zhu et al., 2003). As the FS deviation angle increases, the windbreak effectiveness of the FS gradually decreases (Zhu, 2023) (Fig. A6). The FS deviation angle can be up to 30° without significantly reducing its protective effect, whereas a deviation of 45° noticeably weakens its effectiveness. Therefore, to account for other construction requirements, the construction orientation of a primary FS can have a maximum deviation angle of up to 45° during actual implementation (National Forestry and Grassland Administration, 2013; Zhu, 2023). In this study, we divided the FS deviation angles at all 163 sites into three categories: excellent (less than 30°), good (greater than 30° but less than 45°), and poor (greater than 45°).

The wind frequency and directional distribution (across 16 directions: N, NNE, NE, ENE, E, ESE, SE, SSE, S, SSW, SW, WSW, W, WNW, NW, and NNW) were compiled from daily continuous observations. The dominant harmful wind direction was identified as that with the highest frequency among these 16 directions. Only winds with speeds greater than 5 m/s were included in the analysis, as winds exceeding this threshold are capable of mobilizing sand particles (Ma et al., 2024).

The FS orientations within a 50 km × 50 km grid around each meteorological station (the four 25 km × 25 km grids closest to the station) were categorized into 10-degree intervals. The primary FS orientation was determined on the basis of the most frequent orientation, whereas the secondary FS orientation was defined as the direction with the highest frequency among those that do not form clusters with the primary FS orientation. We did not directly consider the second-most-frequent orientation as the secondary FS orientation. In FS design, primary and secondary orientations are often nearly perpendicular to each other to maximize protective effects. However, when FS orientations within a region were analyzed, the top few most frequent orientations were often clustered around the primary FS orientation, making them unrepresentative of the true secondary FS orientation.

Based on the dominant harmful wind direction in the region and the primary and secondary FS orientations, the deviation angles for the primary and secondary FSs were calculated separately. The smaller of the two deviation angles was selected as the FS deviation angle for the region, because the smaller deviation angle serves as a better indicator of the region's wind protection performance against dominant harmful wind.

3.4. Accuracy assessment

3.4.1. Model performance

Traditional metrics were calculated, including precision, recall, F1-score, intersection over union (IoU), and overall accuracy (Eqn 11, 12, 13, 14 and 15). These metrics were used to evaluate the performance of the model on the testing dataset, providing insight into the model's classification accuracy.

$$Precision = TP/(TP + FP) \tag{11}$$

$$Recall = TP/(TP + FN) \tag{12}$$

$$F1\ Score = 2 \times Precision \times Recall/(Precision + Recall) \tag{13}$$

$$IoU = TP/(TP + FP + FN) \tag{14}$$

$$Overall\ Accuracy = (TP + TN)/(TP + TN + FP + FN) \quad (15)$$

where TP refers to true positives, i.e., the actual value is positive and the predicted value is also positive; TN refers to true negatives, i.e., the actual value is negative and the predicted value is also negative; FP refers to false positives, i.e., the actual value is negative but the predicted value is positive; and FN refers to false negatives, i.e., the actual value is positive but the predicted value is negative.

3.4.2. Map accuracy

Validation was carried out at multiple levels: independent assessments were performed for both raster- and vector-based FS products, official FS area statistics from government agencies were used for external validation, and UAV data provided localized validation.

3.4.2.1. Pixel-based. The raster format FS map derived from satellite imagery contains prediction errors and biases (Olofsson et al., 2014; Skakun, 2025). To obtain an unbiased accuracy assessment, a confusion matrix was constructed based on the stratified validation samples described in Section 2.3.2. Following the good practice guidelines proposed by Olofsson et al. (2014), a post-stratified estimator was applied to convert the matrix into unbiased accuracy metrics. The uncertainty of the estimated accuracies was quantified using a 95 % confidence interval (CI).

3.4.2.2. Object-based and length-weighted. These validations were conducted using the reference data described in Section 2.3.2, which was specifically designed for assessing the vector format FS product.

Traditional one-to-one matching metrics are unsuitable for vector-level validation due to FS fragmentation. Therefore, we adopted a many-to-one matching strategy. According to Lei and Lei (2024), both object-based and length-weighted matching metrics were used to assess FS vector format results. Each FS was treated as an individual object, and a match was established between the reference and extracted datasets when the center of an FS in one dataset was within 30 m of an FS in the other. Matched FSs in the reference and extracted data were recorded as true positives with respect to the reference (TP_r) and the extraction (TP_e), respectively.

In this context, object-based recall ($Recall_o$) was defined as the proportion of reference FS objects that were successfully matched (TP_r), while object-based precision ($Precision_o$) was the proportion of extracted FS objects that were successfully matched (TP_e). We defined false positives (FP_o) as unmatched extracted FS objects, and false negatives (FN_o) as unmatched reference FS objects. The overall object-based matching quality is quantified using an adapted $F1\ Score_o$ (Eqn 16, 17 and 18).

$$Precision_o = TP_e/(TP_e + FP_o) \quad (16)$$

$$Recall_o = TP_r/(TP_r + FN_o) \quad (17)$$

$$F1\ Score_o = 2 \times Precision_o \times Recall_o/(Precision_o + Recall_o) \quad (18)$$

We further introduced length-weighted matching metrics, where counts were replaced by the corresponding FS object lengths. Length-weighted precision ($Precision_l$) measured the proportion of the total length of correctly matched FSs in the extracted data, whereas length-weighted recall ($Recall_l$) denoted the proportion of the total length of correctly matched FSs in the reference data (Eqn 19, 20 and 21).

$$Precision_l = L_{TPe}/(L_{TP_e} + L_{FP_o}) \quad (19)$$

$$Recall_l = L_{TPr}/(L_{TP_r} + L_{FN_o}) \quad (20)$$

$$F1\ Score_l = 2 \times Precision_l \times Recall_l/(Precision_l + Recall_l) \quad (21)$$

Additionally, we performed regression analysis between the FS lengths from the extracted and reference data to quantify bias and assess overall agreement. The coefficient of determination (R^2) and root mean square error (RMSE) were calculated. This regression model was also used to correct the bias in FS length estimation.

Table 1
Model accuracy by subregion. (For evaluating model performance).

AEZ	Precision	Recall	F1-Score	IoU	OA
North East China	79.93 %	82.25 %	80.88 %	68.18 %	97.54 %
Inner Mongolia	85.20 %	80.33 %	82.53 %	70.33 %	98.13 %
Huang-Huai-Hai	74.37 %	82.22 %	77.86 %	63.83 %	98.20 %
Loess region	65.75 %	70.07 %	67.08 %	50.97 %	98.94 %
Gansu-Qinghai	83.31 %	81.06 %	82.16 %	69.92 %	98.48 %
Xinjiang	87.41 %	80.33 %	83.71 %	72.06 %	97.31 %

3.4.2.3. Statistic-based. We conducted a linear regression analysis between the extracted FS areas and the statistical data collected from several provinces and cities. The coefficient of determination (R^2) and root mean square error (RMSE) were calculated to evaluate the agreement and quantify the estimation error.

3.4.2.4. UAV-based local validation. The high-resolution UAV imagery provided detailed ground observations, enabling local validation within the survey areas. A total of 210 validation pixels were sampled within these areas, including 100 pixels of FS and 110 of non-FS for pixel-based validation (same methodology as described in section 3.4.2.1). In addition, FS vectors were manually interpreted for the entire UAV-covered area and fully used for both object-based and length-weighted accuracy assessment (same methodology as described in section 3.4.2.2).

4. Results

4.1. Accuracy assessment

4.1.1. Model performance

The TransUNet model achieved an average F1-score of 79.04 %, with average precision of 79.33 %, recall of 79.38 %, IoU of 65.88 %, and OA of 98.10 %. Notably, the model achieved higher accuracy in Northeast China, Inner Mongolia, Gansu-Qinghai, and Xinjiang, with F1-scores exceeding 80 % in these regions. In contrast, performance was lower in the Huang-Huai-Hai region (77.86 %) and especially in the Loess region (67.08 %), as shown in Table 1.

To better interpret the model's decision-making process, we employed Gradient-weighted Class Activation Mapping (Grad-CAM) (Selvaraju et al., 2020), which is a widely used visualization technique that produces class-discriminative heatmaps based on the gradients of the target class flowing into the last convolutional layer. This enables the identification of spatial regions that contribute most to the model's prediction. Grad-CAM visualizations revealed that the model's highest activations (indicated by red regions) predominantly coincided with linear FS features. The spatial alignment between activation hotspots and elongated FS patterns indicated that linear geometries were associated with the model's classification decisions (Fig. 5).

4.1.2. Map accuracy

4.1.2.1. Pixel-based. For the raster results, the producer's accuracy for the FS class was 79.39 % ± 2.12 %, and the user's accuracy was 79.20 % ± 2.52 %, with an overall accuracy (OA) of 98.25 % ± 0.55 % for the entire map (Table 2). As FSs constitute fine-scale, fragmented features with limited spatial extent, minor positional deviations or boundary uncertainties can have a significant effect on the computed accuracy indicators (Lei and Lei, 2024; Muro et al., 2025).

4.1.2.2. Object-based and length-weighted. The object-based match metrics gauge the degree of agreement between the extracted FSs and

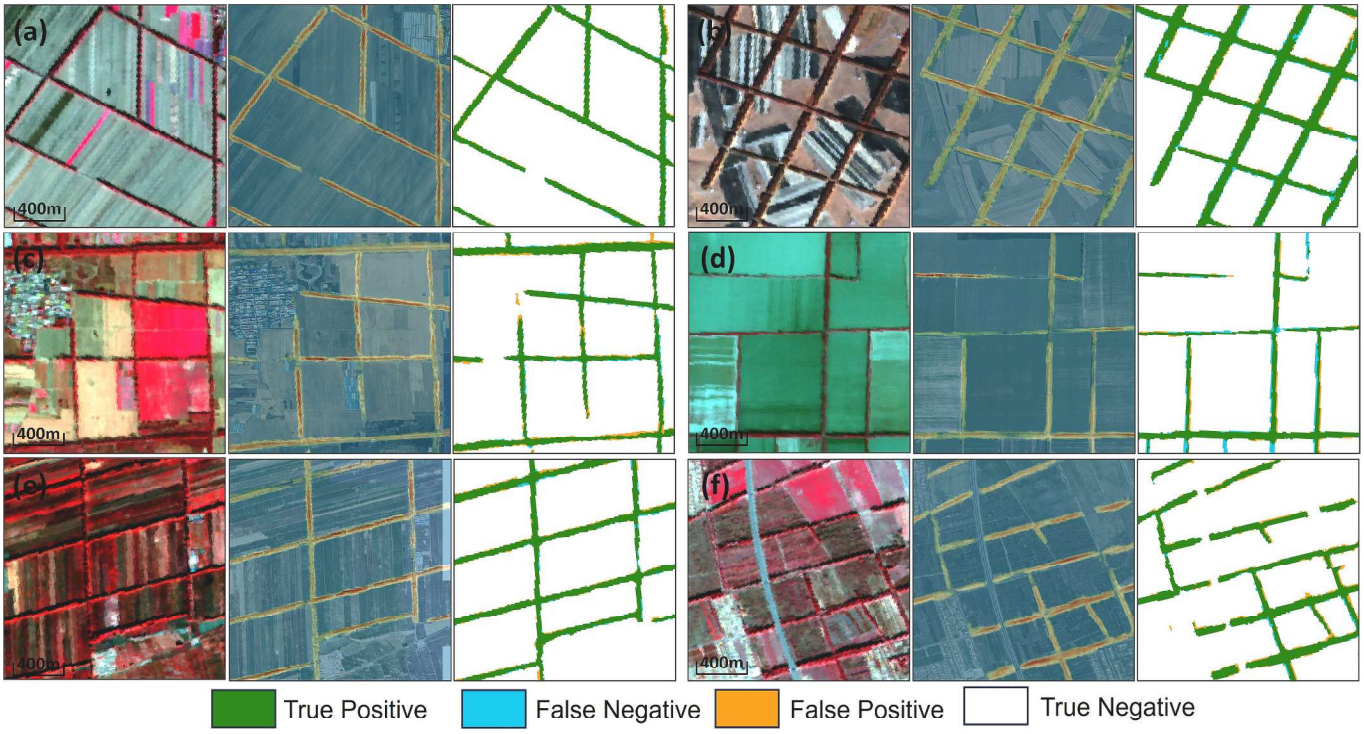


Fig. 5. Sentinel-2 images from the testing dataset, Grad-CAM visualizations generated from the last decoder layer (with the strongest activation highlighted in red; basemap: Google Earth imagery), and corresponding prediction results with highlighted errors for each region: (a) Northeast China, (b) Inner Mongolia, (c) Huang-Huai-Hai, (d) Loess region, (e) Gansu-Qinghai, and (f) Xinjiang. (For interpretation of the references to colour in this figure legend, the reader is referred to the web version of this article.)

Table 2
Map accuracy (pixel-based).

	Reference			
Map class	Absence of FS	Presence of FS	Total	W_i
	Confusion matrix, sample counts			
Absence of FS	1090	10	1100	0.9577
Presence of FS	208	792	1000	0.0423
	Confusion matrix, area proportions			
Absence of FS	0.9489	0.0087		
Presence of FS	0.0088	0.0335		
	Accuracy estimates			
User's acc.	99.09 % ± 0.56 %	79.20 % ± 2.52 %		
Producer's acc.	98.08 % ± 0.11 %	79.39 % ± 2.12 %		
OA	98.25 % ± 0.55 %			

the reference FSs in terms of the number of correctly identified objects. The result showed average object-based recall and precision were 85.77 % and 85.62 %, respectively, yielding an average F1-score of 84.13 %. These values were higher than those of the pixel-based metrics, indicating that the model was effective at identifying and delineating FS objects, even if some pixel-level discrepancies or boundary inaccuracies existed.

In comparison, the length-weighted metrics describe the degree of agreement based on the length of the corrected identified FSs. In our results, average length-weighted recall and precision reached 91.74 % and 89.97 %, respectively, with an average F1-score of 89.62 %. The higher performance of the length-weighted metrics compared with the object-based metrics suggested that, although some smaller or fragmented FSs may be missed or misclassified, the majority of FS length—particularly the longer and more continuous features—had a higher likelihood of being correctly identified.

A linear regression analysis was performed between the extracted FS lengths and the reference FS lengths across validation samples (Fig. 6a). The regression revealed a significant positive relationship, with an equation of $y = 0.99x$, a coefficient of determination (R^2) of 0.89, and a root mean square error (RMSE) of 2.08 km. The regression analysis provided an aggregated and smoothed evaluation of the FS length extraction, which was less affected by local mismatches. Recent studies have shown that such aggregation reduces error rates at coarser scales, as false positives and negatives tend to cancel each other out, resulting in more robust estimates (Muro et al., 2025; Wadoux and Heuvelink, 2023). In addition to accuracy evaluation, the regression model was used to correct systematic bias. The extracted lengths were slightly overestimated compared to reference lengths, and a correction factor of 0.99 was applied to adjust them.

4.1.2.3. Statistic-based. In terms of the total area of the TNR, the "Construction of the Three-North Shelterbelt System: 40 years Development Report" (National Forestry and Grassland Administration, 2019) reported a total FS area of 1656.1 thousand hectares in the TNR, which closely matches our monitoring estimate of 1575.18 ± 58.76 thousand hectares. This supports the reliability of our region-scale estimation.

For the province (city)-level comparison, due to the scarcity of publicly available provincial (city)-level statistics, we could only conduct a rough comparison (Table A1). Regression analysis ($y = 0.81x$, $R^2 = 0.94$, RMSE = 66.36 kha) indicated a strong correlation between the extracted and reported FS areas (Fig. 6b). The extracted FS areas were generally higher than the reported values. This discrepancy may be attributed to temporal mismatches, differences in statistical scope, and definitional differences.

4.1.2.4. UAV-based local validation. Within the UAV data areas, the FS class achieved a user's accuracy of 93.27 % and a producer's accuracy of 82.51 %, with an overall accuracy of 96.39 %. The object-based F1-score was 91.66 %, and the length-weighted F1-score was 93.63 % (Fig. A3 and A5). These UAV sites, located in the core agricultural areas of

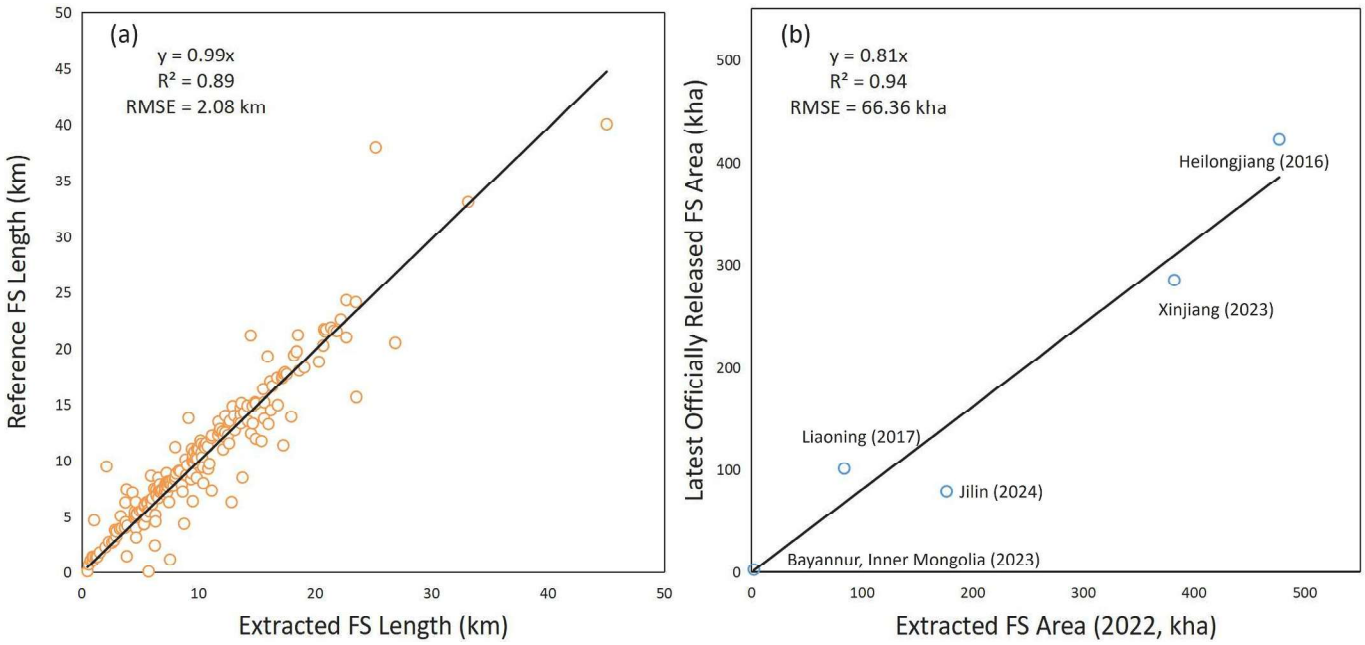


Fig. 6. (a) Extracted lengths vs. reference lengths in sampled grids. (b) Extracted area vs. latest officially released FS area.

Northeast China, suggested relatively high classification performance in this region.

4.2. Distribution of FSs in the TNR

Longitudinally, FSs were concentrated in the eastern and western regions, with a relatively sparse distribution in the central region. Latitudinally, they were mainly concentrated between 40°N and 50°N (Fig. 7).

The total length of the FS system in the TNR was approximately 915.09 ± 21.45 thousand km (Table 3). The length density of FSs in the TNR was approximately 16 m per hectare of farmland. Heilongjiang, Xinjiang, and Inner Mongolia had the longest FS systems, accounting for 29 %, 24 %, and 18 % of the total FS length, respectively (Fig. 9 and Table 3).

The FS width was generally greater in Northeast China, North China plain, and Xinjian. Among these regions, Jilin Province had the widest average FS width, measuring 21.03 ± 1.46 m, particularly in the western region. In Xinjiang, the FS width in the southern region was generally larger than in the northern region (Fig. 8 and Table 3). In regions such as the Hetao Plain, Guanzhong Plain, and Hexi Corridor, FSs tended to be relatively narrow and exhibit discontinuities (Fig. 8).

The total FS area in the TNR was 1575.18 ± 58.75 kha (Table 3). The three provinces with the largest FS area were Heilongjiang (476.83 ± 41.97 kha), Xinjiang (381.99 ± 28.25 kha), and Inner Mongolia (273.34 ± 24.88 kha), whereas the three with the smallest FS areas were Beijing (8.31 ± 0.69 kha), Tianjin (11.57 ± 1.24 kha), and Qinghai (14.42 ± 1.52 kha) (Table 3 and Fig. 9).

4.3. Landscape indicators of FSs

The average FS to farmland ratio in the TNR was 2.83 % ± 0.11 % (Fig. 10 and Fig. 11). At the 25 km grid scale, 8 % of the grids had a ratio of less than 1 %, 64 % had a ratio between 1 % and 4 %, 24 % had a ratio between 4 % and 8 %, and 4 % had a ratio greater than 8 %. The average ratio in Xinjiang Province was 4.65 % ± 0.28 %, whereas in Northeast China, it was 2.96 % ± 0.18 %, and in the North China Plain, it was 2.32 % ± 0.45 % (Table 7). In other regions, the average was 2.01 % ± 0.14 %. Large values were predominantly concentrated in Xinjiang, indicating that the FS density in this region was relatively high. With respect to well-facilitated farmland construction, the area occupied by agricultural infrastructure, including FSs, should not exceed 8 % of the agricultural land area (Ministry of Agriculture and Rural Affairs of the People's Republic of China, 2022). At the city scale, Tiemenguan city and Cocodala city had ratios approaching 8 %, indicating that the areas designated for FS construction in these cities were nearing the upper threshold (Fig. 10a).

The average connectivity in the TNR was 0.34 (Fig. 11). The connectivity was highest in Xinjiang and Northeast China, where FSs exhibited good connectivity with few gaps and discontinuities. In contrast, the Gansu–Qinghai region and the Loess region exhibited relatively low connectivity, suggesting that FS networks were less developed in these areas, with most FSs existing as isolated strips rather than forming an integrated network. This also implied that individual FSs may contain more internal gaps and discontinuities.

The FS to farmland ratio and connectivity varied across different regions. In Xinjiang, both the FS to farmland ratio and connectivity were high. In Northeast China and Huang-Huai-Hai, although the FS to farmland ratio was lower than that in Xinjiang, the connectivity remained high. In contrast, both the ratio and connectivity were relatively low in other regions.

The average FS deviation angle in the TNR was 26°, indicating that the FS orientation generally met the standards for wind protection. Among the 13 provinces and municipalities, only Beijing had an average deviation angle greater than 30° (35°), but still less than 45°, which remained within the acceptable range (Table 4). This may be related to the city's development needs. Among the 163 selected sites, 70 % of the FS orientations were rated as excellent (deviation angle <30°), 22 % as good (30° < deviation angle <45°), and 8 % as poor (deviation angle >45°). The sites classified as "poor" were distributed mainly at the edges of plains or oases, where the FS orientations were more irregular (Fig. 12).

5. Discussion

5.1. Model and result comparison

We conducted a comparative analysis of multiple segmentation

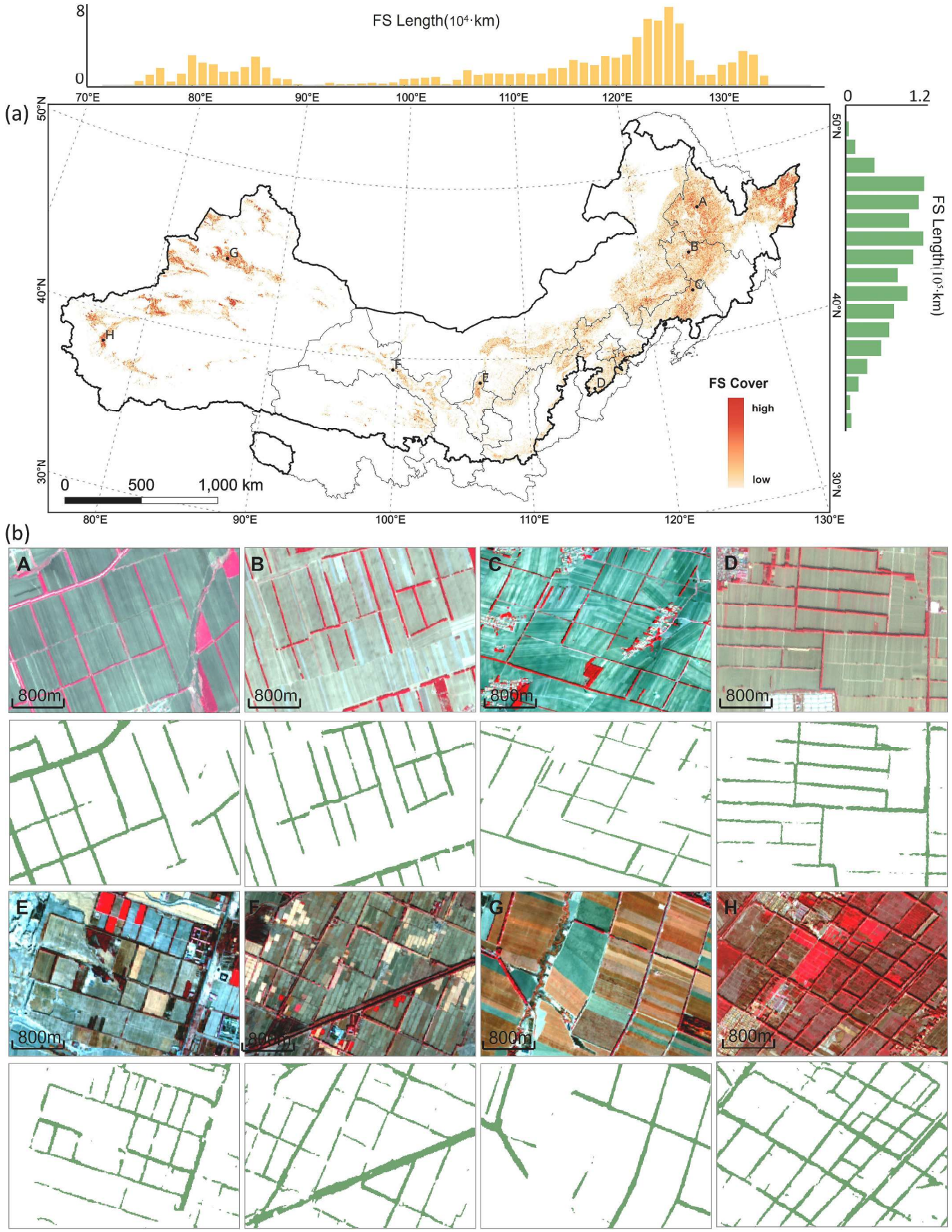


Fig. 7. (a) FS distribution in the TNR. (b) Examples of Sentinel-2 imagery and corresponding extracted FSs.

Table 3
FS length, width, and area in each province.

Province	FS Length(10^3 km)	FS Width(m)	FS Area(10^3 ha)
Heilongjiang	262.85 ± 6.16	18.32 ± 1.54	476.83 ± 41.97
Xinjiang	217.56 ± 5.10	17.74 ± 1.23	381.99 ± 28.25
Inner Mongolia	167.73 ± 3.93	16.46 ± 1.43	273.34 ± 24.88
Jilin	84.63 ± 1.98	21.03 ± 1.46	176.19 ± 13.03
Liaoning	46.09 ± 1.08	18.34 ± 1.27	83.70 ± 6.17
Hebei	41.52 ± 0.97	16.53 ± 1.52	67.96 ± 6.50
Gansu	21.52 ± 0.50	11.85 ± 1.26	25.25 ± 2.77
Shanxi	18.43 ± 0.43	11.61 ± 0.92	21.18 ± 1.77
Ningxia	15.89 ± 0.37	11.92 ± 1.34	18.76 ± 2.18
Shaanxi	14.12 ± 0.33	11.26 ± 1.30	15.74 ± 11.88
Qinghai	10.57 ± 0.25	13.78 ± 1.40	14.42 ± 1.52
Tianjin	9.45 ± 0.22	12.30 ± 1.28	11.57 ± 1.24
Beijing	4.73 ± 0.11	17.75 ± 1.41	8.31 ± 0.69
SUM	915.09 ± 21.45		1575.18 ± 58.75

models to determine which performed better for FS mapping, including UNet (Ronneberger et al., 2015), NL-LinkNet (Wang et al., 2022), VIT (Alexey Dosovitskiy et al., 2021), TransUNet (Chen et al., 2021), Swin-UNet (Cao et al., 2022), and SegFormer (Xie et al., 2021). We also compared the performance of a traditional machine learning model: Random Forest (RF) (Breiman, 2001). The accuracy assessment of different models is shown in Table 5 and Fig. 13.

In general, deep learning models outperformed RF. The RF model exhibited limited capability in distinguishing FSs from forests and orchards, particularly in regions such as Gansu-Qinghai and Xinjiang where FSs are spatially adjacent to orchard landscapes (Fig. 13h). This is likely due to the model's inability to capture the linear morphological characteristics of FSs, instead relying primarily on spectral features, which are relatively similar among these vegetation types and thus leads to misclassification. In contrast, in areas such as Northeast China—where FSs present distinct spectral differences from surrounding farmland—the model achieved relatively higher classification accuracy.

Among deep learning models, TransUNet demonstrated the best performance, while the other two U-shaped networks, Swin-UNet and U-

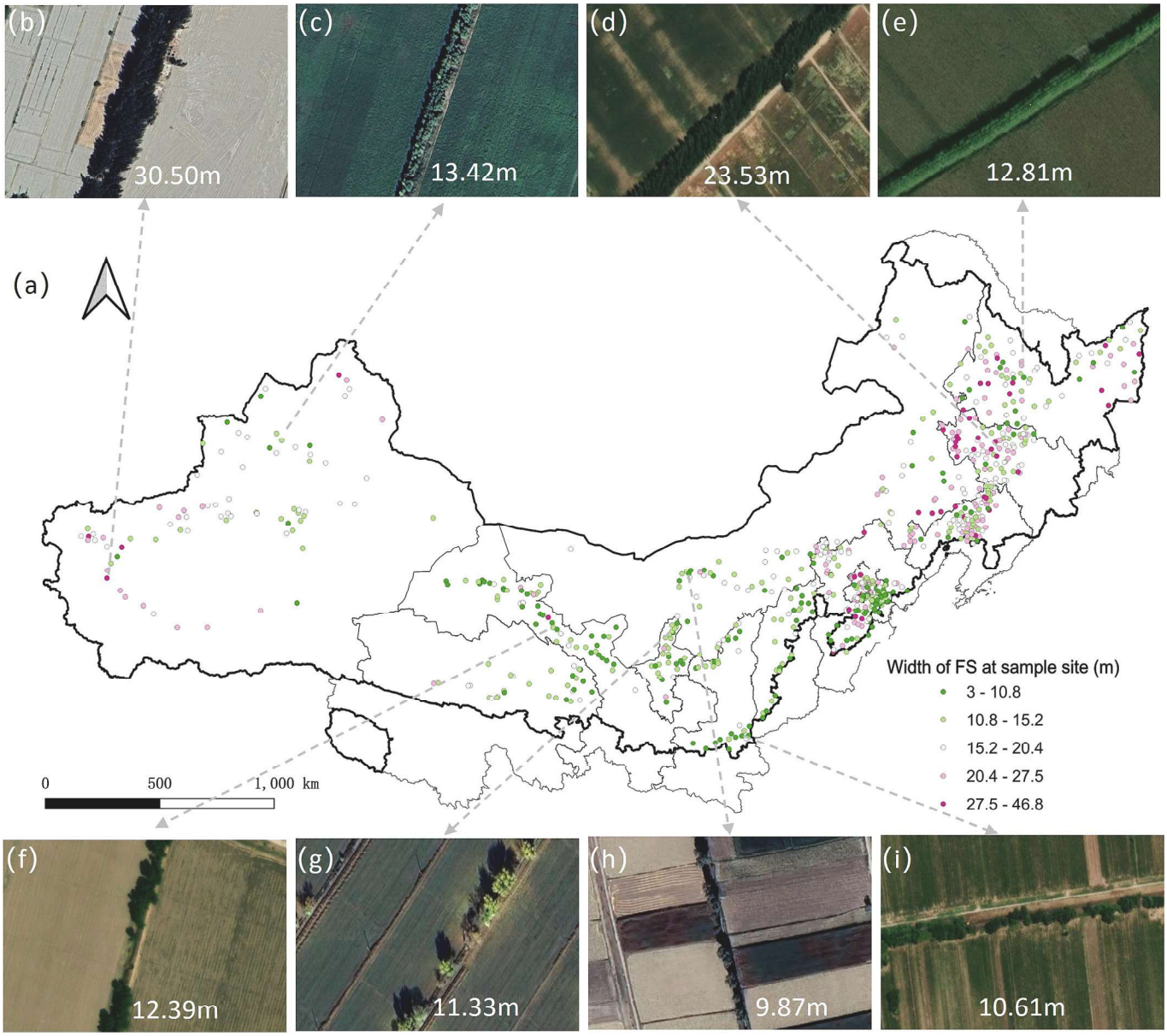


Fig. 8. (a) Sample distribution for FS width estimation. (b–i) Examples of FS sampling points used for width estimation (basemap: Google Earth imagery).

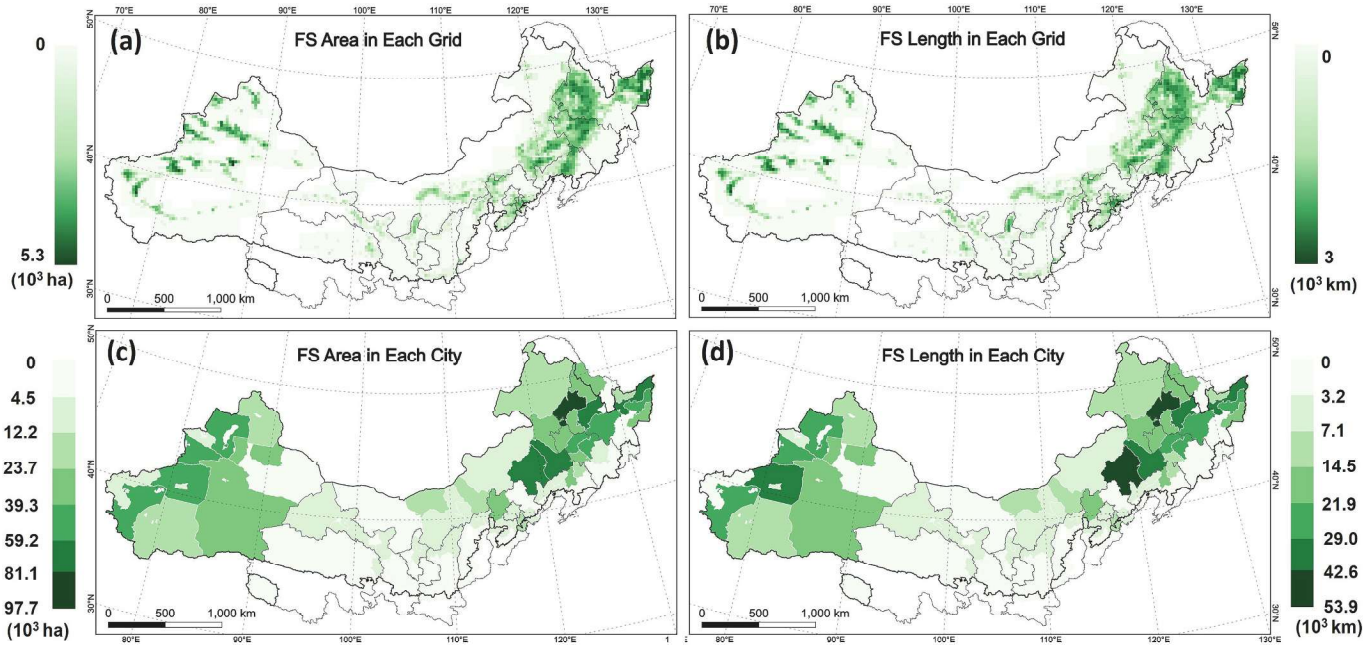


Fig. 9. FS length and area at the 25 km grid (a & b) and at the city level (c & d).

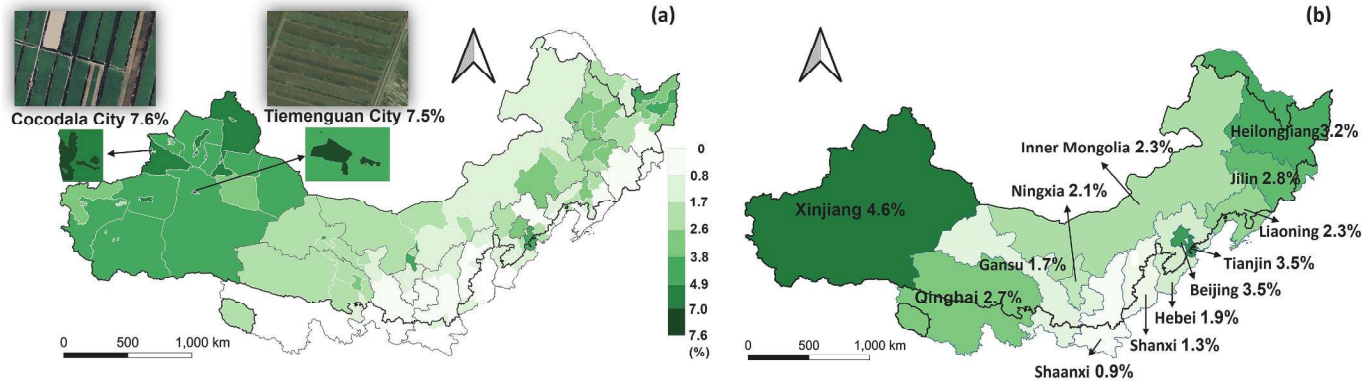


Fig. 10. (a) FS to farmland ratio at the city scale, with Tiemenguan city and Cocodala city having ratios approaching 8 % (satellite images from Google Earth imagery). (b) FS to farmland ratio at the province scale.

Net, also achieved competitive results (Table 5). U-shaped architectures have been shown to be effective in extracting narrow linear vegetation features such as hedgerows (Muro et al., 2025). Specifically, U-Net is a pure CNN model, TransUNet is a hybrid architecture that combines convolution and Transformer modules, and Swin-UNet is a pure Transformer with a U-shaped design (Cao et al., 2022; Chen et al., 2021; Ronneberger et al., 2015). Previous studies suggest that CNNs may be more effective at capturing local features, whereas Transformers are often advantageous in modeling long-range dependencies (Khan et al., 2023; Takahashi et al., 2024). Compared with U-Net, TransUNet incorporates a Transformer encoder into the U-Net backbone, which may allow it to capture global spatial context and long-range dependencies while still retaining CNN-based local detail extraction (Chen et al., 2021). This hybrid design could be particularly beneficial for delineating FSs, which are narrow and elongated features requiring both fine boundary information and global continuity. Swin-UNet leverages shifted window self-attention and a hierarchical encoder–decoder design for efficient multi-scale feature representation (Cao et al., 2022). However, the window-based attention mechanism may limit its ability to capture global dependencies and thus reduce robustness (Qin et al., 2025; Zhou et al., 2022). By integrating global self-attention with convolutional feature extractors, TransUNet may preserve local spatial details while more effectively modeling global dependencies, thereby potentially enhancing robustness and accuracy in this task.

We further compared our results with Zheng et al. (2013), who provided FS length estimates for the TNR up to 2008. In Zheng's study, FS length in Northeast and North China was delineated by manual visual interpretation, whereas in other regions the length was inferred indirectly from a sampling-based statistical relationship between FS length and cropland area. In Northeast and North China (Heilongjiang was not included due to substantial differences in the statistical scope of the region), our extracted FS length showed good agreement with Zheng's estimates ($R^2 = 0.81$, RMSE $= 13.54 \times 10^3$ km), while in other regions the agreement was lower ($R^2 = 0.67$, RMSE $= 60.89 \times 10^3$ km) (Fig. A7). This discrepancy is likely related to differences in the estimation methods: Zheng's estimates outside Northeast and North China relied on indirect extrapolation rather than direct mapping, which may introduce additional uncertainty. In addition, the more heterogeneous distribution of FSs in arid regions likely amplifies this uncertainty. The consistency with visual interpretation in Northeast and North China supports the robustness of our approach and its potential to approximate the accuracy of manual interpretation.

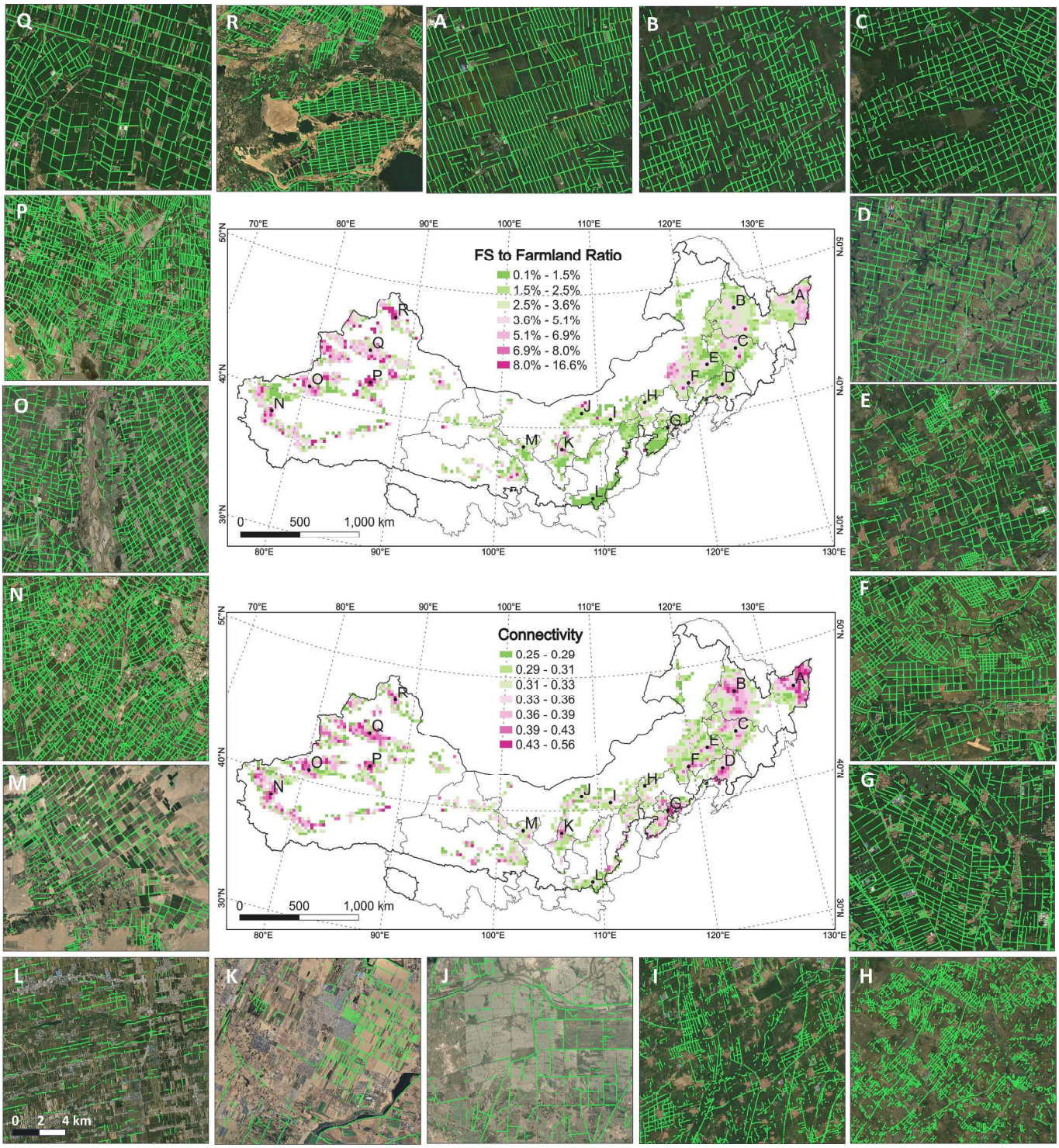


Fig. 11. FS to farmland ratio and connectivity (basemap: Google Earth imagery).

5.2. *Optimal time window for FSs extraction*

Given the varying phenological patterns across ecological zones, we evaluated the influence of different time windows on FS extraction performance across multiple ecological regions.

We constructed NDVI curves for the entire TNR and each AEZ using the 2100-point validation samples. The NDVI values were averaged over 15-day intervals in 2022 (Fig. 14). For FSs, NDVI typically begins to rise in March or April, peaks in August, and then gradually declines, stabilizing after December. Crop types and phenology vary across different regions, leading to distinct NDVI temporal profiles. In Northeast China, Inner Mongolia, Gansu-Qinghai, and Xinjiang, cropland NDVI starts to increase significantly around May, reaches its peak in August, and then decreases, becoming stable after November. In the Huang-Huai-Hai region, which practices double cropping, NDVI rises markedly from March, reaches a first peak in May, declines, increases again in mid-June, and then peaks a second time in August before declining and stabilizing after November. In the Loess region, cropland NDVI increases gradually from March, peaks in August, and then declines, becoming stable after November.

Table 4
Average FS deviation angle in each province.

Province	Average Deviation Angle (°)	Province	Average Deviation Angle (°)
Beijing	35	**Gansu**	21
Hebei	28	**Tianjin**	19
Inner Mongolia	26	**Shanxi**	18
Xinjiang	26	**Shaanxi**	18
Heilongjiang	24	**Jilin**	18
Liaoning	23	**Ningxia**	16
Qinghai	23	**Average of all sites**	26

The main growing season for both crops and FSs spans from May to November, which we further divided into early (May–July), middle (July–September), and late (September–November) growth stages. Sentinel-2 imagery shows that, across all six AEZs, the visual distinction between FS and surrounding farmland is most apparent from September to November (Fig. 14). From May to July, FSs are also relatively distinguishable in Northeast China, Inner Mongolia, and the Huang-Huai-Hai region, but the contrast is less pronounced than in the late growth stage, with weaker textural features. In contrast, from July to September, the distinction is generally weaker.

Models were trained for each growth stage and tested in each AEZ. The highest F1-score was achieved for the late growth stage (Table 6). This period coincides with the harvest season across most regions, during which the contrast between farmland and FS increases, facilitating better discrimination. In Northeast China and Inner Mongolia, relatively good performance was also observed in the early growth stage. In Xinjiang, the middle growth stage also yielded relatively good performance.

5.3. Implications of the TNSFP

FSs operate as interconnected networks that generate synergistic protective effects (Zhu, 2023). The spatial pattern of FSs largely determines their functional benefits. An appropriately designed spatial configuration plays a critical role in enhancing wind reduction efficiency, soil conservation, water regulation, landscape connectivity, biodiversity, and associated ecological processes (Baker et al., 2021; Chang et al., 2019; Gao et al., 2025; Heisler and Dewalle, 1988; Nakahama et al., 2022). Therefore, understanding and optimizing FS spatial patterns is essential for enhancing farmland protection and regional ecosystem services. In this study, we evaluated the spatial pattern of FSs in the Three-North region using three indicators—FS-to-farmland ratio, connectivity, and deviation angle—and provided recommendations for improvement accordingly.

In general, increasing the FS to farmland ratio can enhance wind protection effectiveness (Li and Sherman, 2015). However, when this ratio exceeds a reasonable threshold, the benefits of further increases in the ratio tend to diminish (Li et al., 2020; Sun et al., 2022). Excessively high ratios may even negatively impact agricultural production by occupying excessive farmland and introducing side effects (Zhu et al., 2010). According to the specification for well-facilitated farmland construction, agricultural infrastructure, including FSs, should occupy no more than 8 % of the agricultural land (Ministry of Agriculture and Rural Affairs of the People's Republic of China, 2022). In this study, the average FS to farmland ratio in the TNR was 2.83 %, indicating that there may be room for improvement. However, in areas where the ratio approached 8 %, such as Tiemenguan city and Cocodala city in Xinjiang (Fig. 10a), implementing strategies to maintain a balance between ecological benefits and agricultural land use may be essential. The FS to farmland ratio in southern Xinjiang was relatively high at 4.33 %. However, the average maximum wind speed in this region was comparatively low compared to other key construction regions (Table 7), and water scarcity issues there were more severe (Guo et al., 2025). Thus, it may be worth further investigating the necessity of such a dense FS network and exploring approaches for achieving an optimal balance. Regions such as the Hetao Plain, Hexi Corridor, and Guanzhong Plain, which had lower FS to farmland ratios than other regions with comparable wind speeds (Table 7), present considerable potential for FS expansion, which could enhance environmental stability and agricultural resilience.

Connectivity is an index reflecting network integrity, with low connectivity potentially indicating suboptimal FS configurations and frequent gaps within individual FSs, which may be associated with FS degradation. Wang et al. (2024) found that longer gaps in primary FSs lead to smaller effective protection areas, and that FS networks with complete grid-like structures provide significantly greater wind protection than isolated belts or fragmented configurations, emphasizing the importance of structural integrity in maintaining windbreak functionality. Li et al. (2020) have shown that increased connectivity is positively correlated with cotton yield in arid regions, up to a point where maximum connectivity is achieved. In this study, the average connectivity of FSs across the TNR was estimated at 0.34, which suggests room for structural improvement. This tendency was more evident in regions such as the Guanzhong Plain, Hetao Plain, and Hexi Corridor, where connectivity remained relatively low and fragmented FSs were more common (Fig. 11). Enhancing connectivity in these areas could improve the overall protective effectiveness of the FS network and contribute to more resilient agricultural landscapes.

It is generally recognized that both single FS and FS network provide optimal wind protection when their orientation is perpendicular to the prevailing wind direction (i.e., when the deviation angle is 0°) (Zhu et al., 2003). As the deviation angle increases, the wind protection effectiveness gradually declines (Zhu et al., 2003) (Fig. A6). When the deviation angle exceeds 30°, the protective effect declines significantly, and angles greater than 45° are generally considered unsuitable for effective windbreak performance (Li et al., 2020; Zhu, 2023; Zhu et al., 2003). In this study, the average FS deviation angle across the sites in the TNR was estimated at 26°. In particular, within plains and oasis agricultural areas, the deviation angle was generally less than 30°, which allowed the FSs to maintain effective wind protection capacity (Fig. 12). However, we found that deviation angles tended to be larger at the edges of plains and oasis agricultural areas, primarily because FSs in these transitional zones are more irregular in orientation, and lack a consistent directional pattern. In future construction efforts, additional consideration may be needed in these regions to enable FSs to function at their best in terms of wind protection.

In addition, we compared our extracted FS area with the planned FS area to evaluate the construction status of farmland shelterbelts within the framework of the project. We chose to use the Phase IV planning data because it is the most recent publicly available dataset that provides province-level FS construction targets (National Forestry and Grassland Administration, 2001), and the total planned FS area during Phase IV was 1110.1 thousand hectares, which is comparable to the 1656.1 thousand hectares reported in "Construction of the Three-North Shelterbelt System: 40 years Development Report" (National Forestry and Grassland Administration, 2019), suggesting that Phase IV may represent a critical period for large-scale FS establishment (Heilongjiang Province was excluded from the comparison due to a substantial mismatch between our study area and the official Phase IV planning boundaries).

Jilin and Inner Mongolia have already exceeded their Phase IV planned FS areas (Fig. 15). These two provinces were designated as key construction zones at the initial stage of the TNSFP, and much of their FS development was completed prior to Phase IV (National Forestry and Grassland Administration, 1978, 1986, 1996). Therefore, these regions may need to shift their focus from simply increasing the number of shelterbelts to the renewal, maintenance, and optimization of the existing FS layout, as well as to strengthening construction in locally

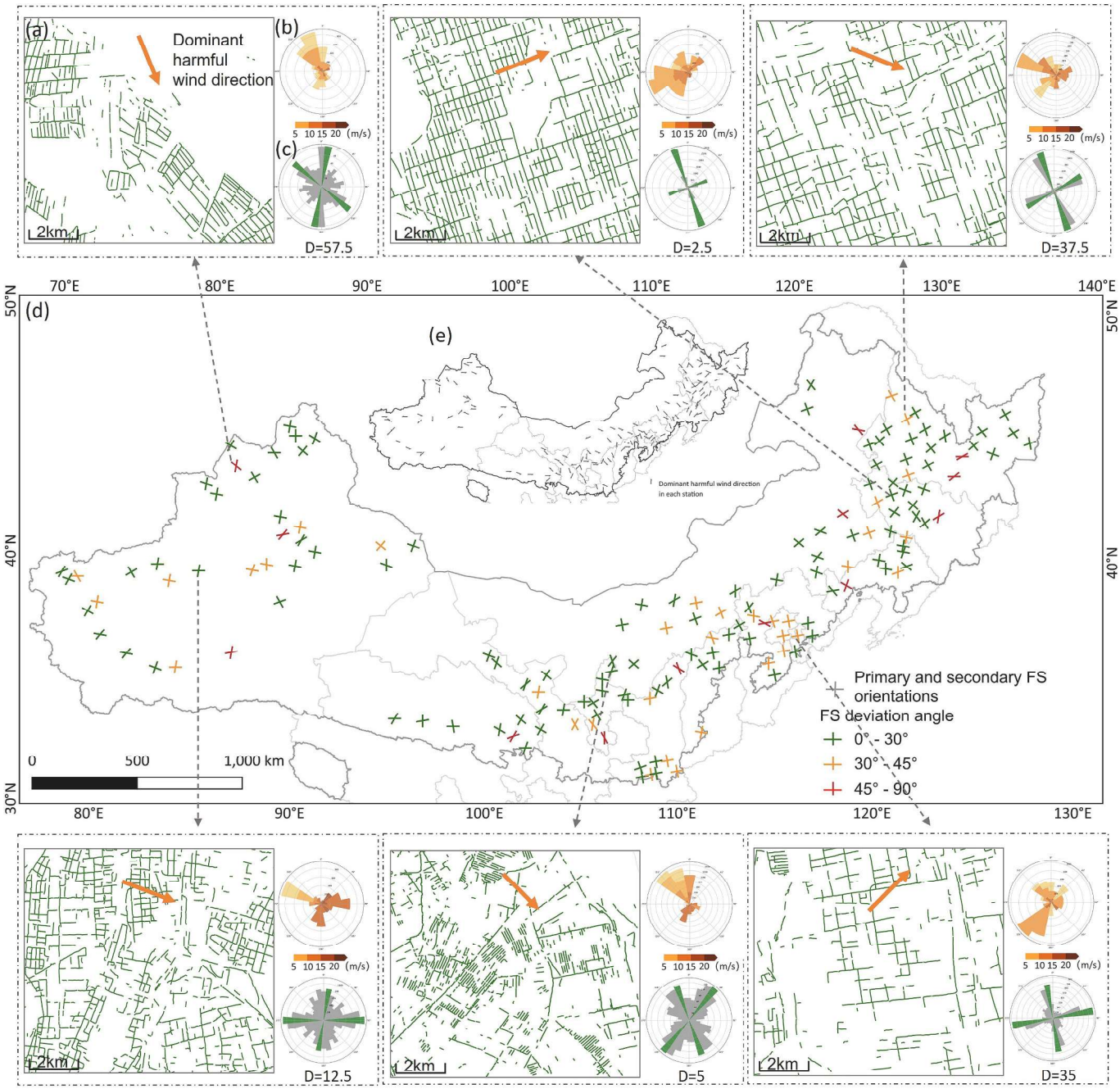


Fig. 12. (a) Detailed information about the FS network in this region. (b) Sandstorm wind rose diagram for the station. (c) Frequency distribution of FS orientations in the region, with the primary and secondary FS orientations highlighted in green. Under figure (c) `D` represents the FS deviation angle in this region (°). (d) FS orientations and FS deviation angles calculated within a 50 km × 50 km grid surrounding each meteorological station. In the diagram, each "+" symbol represents a station, with the two arms indicating the primary and secondary FS orientations in this region. The symbol colour is categorized into three levels, which correspond to the FS deviation angle in this region. (e) The single-sided gray arrow represents the direction of the dominant harmful wind in each station. (For interpretation of the references to colour in this figure legend, the reader is referred to the web version of this article.)

Table 5
Accuracy assessment of different models.

	Precision	Recall	F1-Score	IoU	OA
TransUNet	79.33 %	79.38 %	79.04 %	65.88 %	98.10 %
Swin-UNet	73.89 %	78.84 %	75.32 %	61.46 %	97.80 %
SegFormer	78.61 %	72.78 %	75.24 %	61.15 %	97.87 %
UNet	63.77 %	77.40 %	68.09 %	53.19 %	97.01 %
NL-LinkNet	71.88 %	61.96 %	65.30 %	49.81 %	97.22 %
VIT	61.51 %	60.27 %	58.68 %	42.78 %	96.37 %
RF	21.34 %	82.40 %	31.28 %	19.63 %	80.58 %

underdeveloped areas, such as the Hetao Plain in Inner Mongolia. Conversely, in provinces such as Ningxia, Liaoning, Xinjiang, Shaanxi, Shanxi, and Qinghai, the FS areas by 2022 had not yet reached the targets set during Phase IV (Fig. 15), which may indicate the potential need for continued FS construction. Especially in regions such as Ningxia, Shaanxi, and Shanxi, this shortfall may be attributed to FS degradation, as these areas also exhibit notably low connectivity—potentially reflecting the presence of degraded FS with internal breaks. However, in Xinjiang, the planning of new FSs should be approached with caution to balance FS area with available cropland, and to ensure a sustainable



Fig. 13. Examples of classification results and errors of different models on the test dataset: (a) Sentinel-2 Images of the test dataset, (b) TransUNet, (c) Swin-UNet, (d) SegFormer, (e) UNet, (f) NL-LinkNet, (g) ViT, and (h) RF.

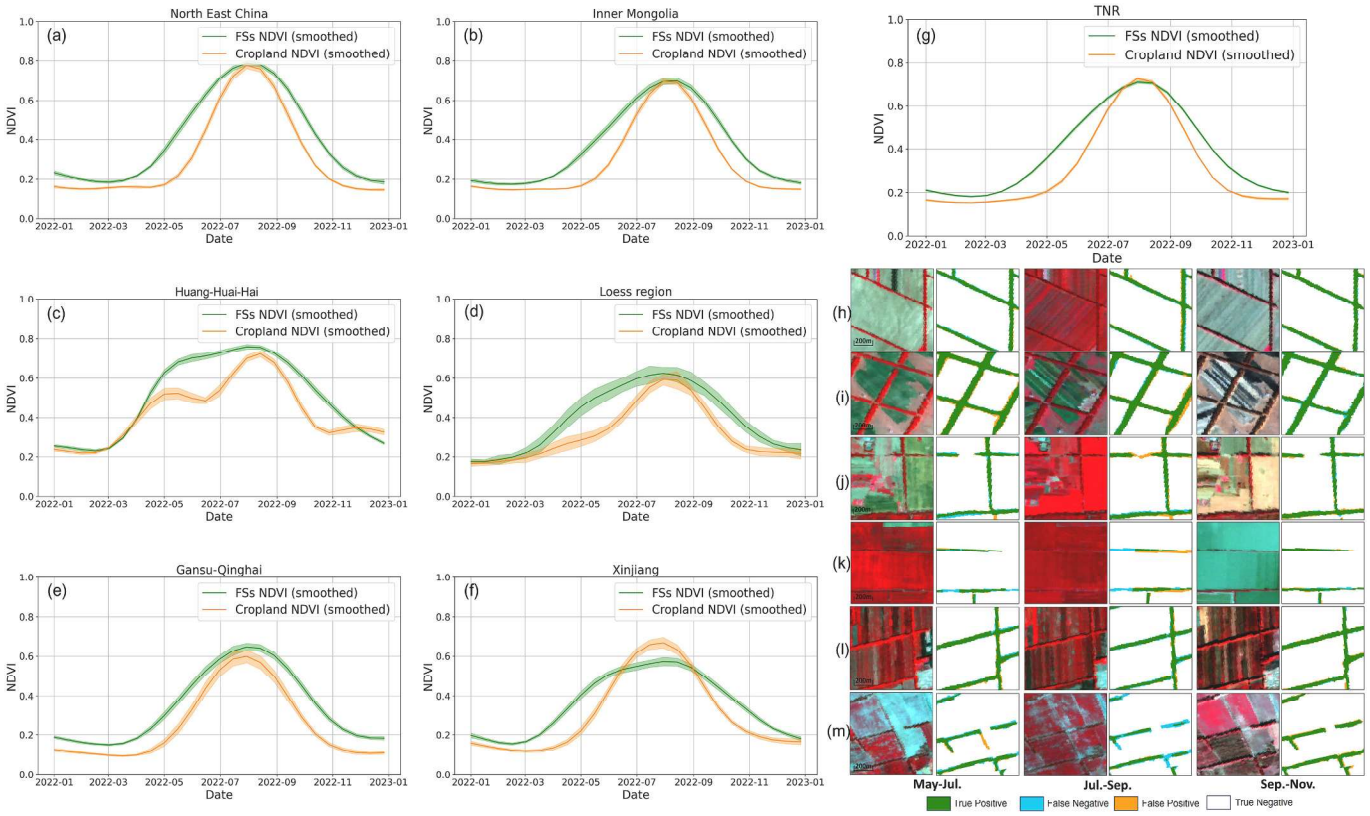


Fig. 14. (a-g) NDVI Curves of FSs and Farmland for the TNR and AEZs in 2022. (h-m) Examples of Sentinel-2 composite images and corresponding error maps at different growth stages for each AEZ: (h) Northeast China, (i) Inner Mongolia, (j) Huang-Huai-Hai, (k) Loess region, (l) Gansu-Qinghai, and (m) Xinjiang.

Table 6
Accuracy assessment at different growth stages for each AEZ.

AEZ	May-Jul.	Jul.-Sep.	Sep.-Nov.
North East China	**73.22 %**	69.44 %	**80.88 %**
Inner Mongolia	**73.69 %**	71.53 %	**82.53 %**
Huang-Huai-Hai	62.93 %	62.34 %	**77.86 %**
Loess region	56.83 %	48.31 %	**67.08 %**
Gansu-Qinghai	70.26 %	64.47 %	**82.16 %**
Xinjiang	73.18 %	**76.12 %**	**83.71 %**
The TNR	68.35 %	65.37 %	**79.04 %**

Table 7
FS to farmland ratio and average maximum wind speed in key FS construction regions.

Region	FS to farmland ratio	Average Maximum Wind Speed (m/s)
Hetao Plain	**2.22 %**	**10.26**
Sanjiang Plain	3.37 %	10.07
Hexi Corridor	**1.76 %**	**9.97**
Northern Xinjiang	4.94 %	9.94
Liaohe Plain	2.53 %	9.57
Songnen Plain	2.71 %	9.50
Southern Xinjiang	**4.33 %**	**8.78**
Guanzhong Plain	**0.70 %**	**8.70**
North China Plain	2.32 %	8.66

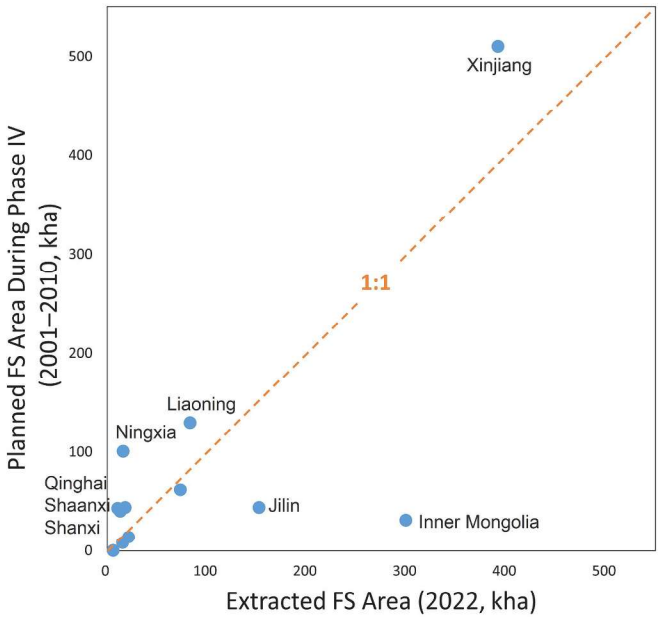


Fig. 15. Extracted FS area in 2022 vs. planned FS area during Phase IV.

trade-off between ecological and agricultural use.

FSs play significant protective roles for crops in agricultural fields. Cai et al. (2021) reported that FSs can mitigate crop lodging caused by typhoons. We also conducted a preliminary qualitative analysis of a 2020 typhoon event in Northeast China, during which widespread crop lodging was observed. In certain local areas, we observed that locations at the periphery of the FS network—where FSs were sparser and connectivity was lower—may have experienced more severe lodging compared to areas with denser and better connected FSs (Fig. A8) (since the changes in FSs over two years were minimal, the 2022 FS map was used for analysis; the lodging data were obtained from previous research conducted by the research team). Therefore, clarifying and optimizing the spatial patterns of FSs in the TNR holds significant guiding

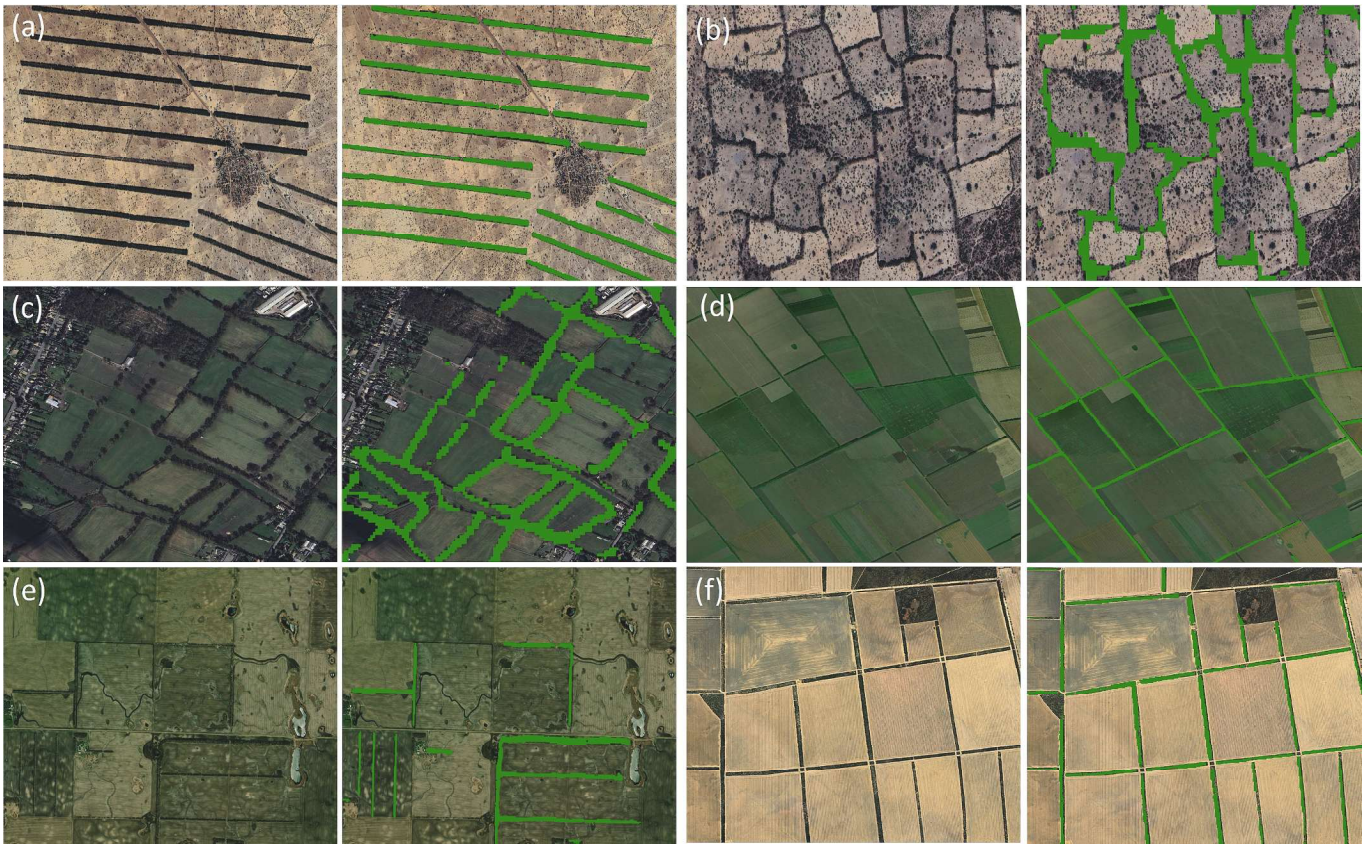


Fig. 16. Examples of shelterbelt extraction performance across different global regions (basemap: Google Earth imagery). (a, b) Shelterbelts in the Great Green Wall (Northern Nigeria, 12.490669°N, 8.083163°E), showing (a) planted shelterbelts and (b) semi-natural shelterbelts retained around farmland. (c) Hedgerows in Europe (United Kingdom, 52.353846°N, 1.829647°W). (d) Shelterbelts in the Ukrainian plains (49.026898°N, 34.874456°E). (e) The Great Plains Shelterbelt Project in the United States (47.47959°N, 97.69589°W); (f) Shelterbelts in Australia (31.540856°S, 119.173656°E). (For interpretation of the references to colour in this figure legend, the reader is referred to the web version of this article.)

importance.

These mapping efforts can play a role in the dynamic adjustment of TNSFP policies. By providing detailed spatial distribution and structural information of existing FSs, the mapping results enable policymakers to assess the effectiveness of previous investments and identify critical gaps, thereby supporting the optimization of future construction planning. This spatial intelligence supports a more flexible, adaptive, and region-specific policy framework. For example, based on the above analysis, future planning of FS construction may need to consider increasing the FS to farmland ratio and connectivity in the Guanzhong Plain, Hetao Plain, and Hexi Corridor, while also taking measures to reduce the risk of FS degradation. In Xinjiang, greater attention may be needed to ensure a reasonable FS to farmland ratio and to avoid potential overuse of farmland and other resources. Greater attention may also need to be given to the orientation of shelterbelts at the margins of agricultural areas to ensure that they can achieve optimal wind protection effectiveness.

5.4. Global applicability of the method

Similar shelterbelts have been established in various regions around the world. Based on samples collected from representative global regions, we evaluated the global transferability of this method. The results demonstrated that this mapping approach performed well in extracting FSs globally and showed strong scalability. Specifically, the extraction results were most accurate in the Ukrainian plains (Fig. 16d), where the shelterbelt networks were spatially regular. In contrast, performance declined in certain African regions characterized by narrow, semi-natural forest strips surrounding farmland (Fig. 16b). These results suggested that the model was generally effective at a global scale, but spatial heterogeneity in accuracy remained.

5.5. Potential contributions

This study has several potential contributions. First, this study proposed a deep-learning framework for extracting FS spatial patterns from medium-resolution Sentinel-2 imagery, enabling large-scale and automated detection of linear vegetation features. Second, this study generated a comprehensive vectorized FS network that integrates individual FS attributes with landscape metrics, allowing for both fine-scale structural analysis and broader landscape characterization. Third, this study provided a systematic quantification of FS spatial patterns across the TNR, offering new insights into regional differences in FS distribution. These contributions offered valuable guidance for future dynamic monitoring of FSs over time and provided methodological support for scaling up similar monitoring efforts to other regions globally.

5.6. Limitations and prospective

This study successfully generated and validated a FS map and a vectorized FS network for the TNR using Sentinel-2 imagery at 10-m resolution. In addition, this study analyzed the spatial patterns of FSs across the TNR. Nevertheless, several limitations remain in this study.

The accuracy of the model varies across different regions due to variability in FS landscape types. According to the accuracy assessment in section 4.1.1, the overall extraction performance remains relatively high, with an average F1-score exceeding 79.04 %. The model achieved higher accuracy in Northeast China, Inner Mongolia, Gansu-Qinghai,

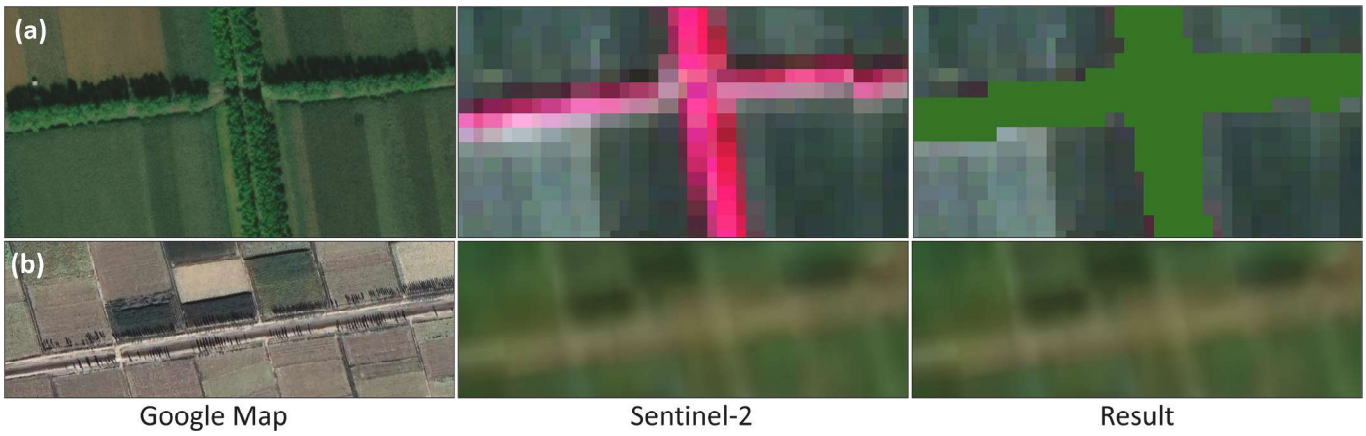


Fig. 17. Examples of the limitations of this study (basemap: Google Earth imagery). (a) Boundary inaccuracies caused by mixed pixels. (b) Omission of extremely narrow FSs.

and Xinjiang, with F1-scores exceeding 80 % in these regions. In contrast, performance was lower in the Huang-Huai-Hai region (77.86 %) and especially in the Loess region (67.08 %). The reduced performance may be attributed to several factors: In the Loess region, FSs are relatively sparse, scattered, narrow, and frequently fragmented, along with the presence of numerous block-shaped forest patches that interfere with accurate identification. These FSs may be challenging to distinguish, even in high-resolution imagery (Fig. 17b). In Huang-Huai-Hai, the landscape is complex, with croplands being fragmented and scattered due to urban expansion, which increases the difficulty of FS extraction. The difficulty in accurately extracting FSs due to their scattered, discontinuous, and intermixed distribution was also reported in previous studies (Lechner et al., 2009; Muro et al., 2025). Potential solutions to these challenges include improving deep learning models to better capture small and narrow landscape features and refining stratified sampling approaches to enhance the representativeness of training samples. In this study, stratification based on AEZs and cropland proportion produced a relatively balanced sample distribution. Nevertheless, more refined stratification schemes may offer additional benefits.

Data quality and spatial resolution are critical factors in FS extraction. Although we utilized Sentinel-2 imagery, which provides relatively high spatial resolution among publicly available satellite datasets, and deep learning models were able to accurately extract most FSs from this dataset, the method cannot fully compensate for inherent resolution limitations. The restricted resolution imposes two main challenges: boundary inaccuracies and omission of extremely narrow FSs. Mixed pixels often lead to imprecise delineation of FS boundaries (Fig. 17a), while extremely narrow FSs are prone to omission (Fig. 17b). High-resolution imagery offers more precise delineation and improved detection of narrow FSs, providing a promising direction for enhancing FS mapping accuracy. For FSs in the Loess region, higher-resolution remote sensing data may greatly enhance extraction accuracy.

The deviation angles in this study were calculated according to each region's dominant harmful wind direction, broadly following the recommended practice in farmland shelterbelt construction standards (National Forestry and Grassland Administration, 2013; Ministry of Agriculture and Rural Affairs of the People's Republic of China, 2022). Although this approach effectively evaluates regional-scale FS orientation suitability, it fails to account for the influence of local environmental factors. Specifically, topography, land use characteristics, and microclimate-driven wind patterns may influence FS orientation and its resulting protective effectiveness. For instance, in the oasis margins of Xinjiang, FSs may be required to defend against winds from multiple directions due to frequent sandstorms not only the dominant harmful wind. Consequently, future FS orientation assessments would benefit from the inclusion of local environmental factors.

6. Conclusion

This study introduced a deep learning-based framework using TransUNet and Sentinel-2 data to extract and analyze the spatial patterns of FSs in the TNR at 10-m resolution for 2022. The results indicated that the total FS length was approximately 915.09 ± 21.45 thousand km, and the total area was 1575.18 ± 58.75 thousand ha in the TNR. The average FS to farmland ratio was 2.83 % (± 0.11 %), with values approaching 8 % in Tiemenguan city and Cocodala city, highlighting the need to balance ecological benefits and agricultural land use. The average FS connectivity was 0.34, indicating room for optimization, especially in the Hetao Plain, Hexi Corridor, and Guanzhong Plain. The average FS deviation angle was 26°, suggesting well-aligned orientations with good wind protection efficiency. The final FS map demonstrated high accuracy under different evaluation perspectives. Specifically, the pixel-based user's accuracy was 79.20 %, and the producer's accuracy was 79.39 %; the average object-based F1-score was 84.13 %, and the average length-weighted F1-score was 89.62 %. This study found that the late growth stage was the optimal time for FS extraction, effectively distinguishing FSs from surrounding farmland. A comparative evaluation of multiple models demonstrated that TransUNet outperformed the other models in FS extraction. To our knowledge, this study presents the first 10-m resolution FS map and the first vectorized FS network of the TNR, providing a crucial dataset for evaluating FS spatial patterns, optimizing the FS network, and improving agricultural resilience. The findings offer valuable insights for ecological restoration efforts and sustainable agricultural land management.

CRediT authorship contribution statement

Hui Ma: Writing – original draft, Validation, Software, Methodology, Formal analysis, Data curation. **Bingfang Wu:** Writing – review & editing, Supervision, Resources, Conceptualization. **Fuyou Tian:** Writing – review & editing, Methodology, Data curation. **Hang Zhao:** Data curation. **Yifan Li:** Data curation. **Mengxiao Li:** Data curation. **Miao Zhang:** Writing – review & editing, Data curation. **Hantian Wu:** Data curation. **Hongwei Zeng:** Writing – review & editing. **Liang Zhu:** Data curation.

Declaration of competing interest

The authors declare that they have no known competing financial interests or personal relationships that could have appeared to influence the work reported in this paper.

Acknowledgments

This research was financially supported by the National Key Research and Development Program of China (No. 2024YFD1500604), the National Natural Science Foundation of China (Grant numbers: 41991232), the Third Xinjiang Scientific Expedition (No. 2022xjkk030106), the National Natural Science Foundation of China (Grant numbers: 42461144211), and the Youth Innovation Promotion Association of Chinese Academy of Sciences (2022125).

Appendix A. Appendix

Table A1
The information of the data used in this study.

Data name	Description	Source
Sentinel-2 Level-2A	Sentinel-2 Level-2A provides surface reflectance products with 13 spectral bands. In this study, four bands were used, including the red, green, blue, and near-infrared (NIR) bands, all with a spatial resolution of 10 m.	https://developers.google.com/earth-engine/datasets/catalog/COPERNICUS_S2_SR_HARMONIZED?hl=zh-cn
GF-1 imagery	Chinese high-resolution GF-1 satellite imagery with a spatial resolution of 2 m was provided by National Earth Observation Data Center.	https://noda.ac.cn/datasharing/
ESRI World Imagery	Global high-resolution remote sensing base map (~0.5–2 m), primarily for visual reference.	https://livingatlas.arcgis.com/wayback/
Google Earth imagery	Global high-resolution remote sensing base map (~0.5–2 m), primarily for visual reference.	https://developers.google.com/maps/documentation/maps-static/dev-guide/
UAV data	The UAV imagery was acquired at an altitude of approximately 120 m using a nadir (vertical) camera orientation, with a horizontal positioning accuracy of 3 cm.	Field survey
ESA WorldCover 10 m v200	A global land cover product with a 10 m spatial resolution, covering 11 major land cover classes, was provided by the European Space Agency (ESA).	https://developers.google.com/earth-engine/datasets/catalog/ESA_WorldCover_v200?hl=zh-cn
Official statistics on farmland shelterbelts (FS)	The FS statistics were obtained from the official datasets released by the government's official website. Publicly available data were collected for Jilin, Heilongjiang, Liaoning, Xinjiang, and Bayannur in Inner Mongolia.	**Jilin (2024):** https://jllc.jl.gov.cn/xxfb/xydt/tpxw/202406/t20240604_3200870.html **Heilongjiang (2016):** http://hl.cma.gov.cn/xwzx/kpzc/201607/t20160718_647152_ph.html **Liaoning (2017):** https://lyt.ln.gov.cn/lyt/zfxxgk/fdzdgknr/jyta/srddbjy/2017n/84AD637179DB456ABCBD2D49BD5147DD/index.shtml **Xinjiang (2023):** https://lcj.xinjiang.gov.cn/lcj/mtbd/202310/cce33e4d139f4d36a63e7a4a9b22f8a8.shtml **Bayannur, Inner Mongolia (2023):** https://bynr.gov.cn/dtxw/zwdt/202310/t20231030_571548.html
China's daily meteorological observation dataset	Daily meteorological data, including wind speed and direction, were obtained from observations at meteorological stations provided by the Resource and Environmental Science Data Platform	https://www.resdc.cn/data.aspx?DATAID=230
Integrated Surface Data - "Lite"(ISD-Lite data)	Global meteorological data, including wind speed and wind direction, were provided by the National Centers for Environmental Information (NCEI).	https://www.ncei.noaa.gov/pub/data/noaa/isd-lite/

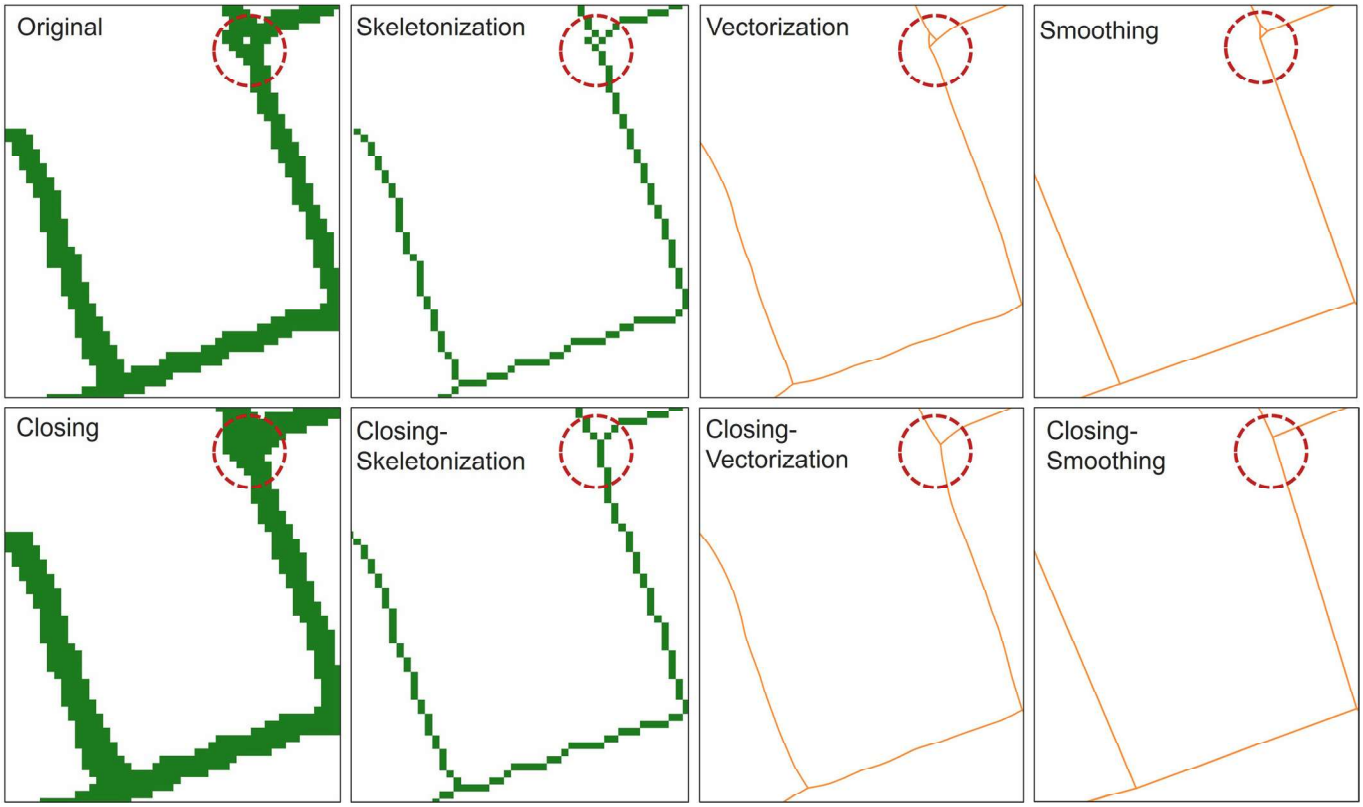


Fig. A1. Examples of postprocessing.

Table A2
The sample size for width estimation in each province.

Province	Sample size
Heilongjiang	78
Xinjiang	78
Inner Mongolia	78
Jilin	82
Liaoning	78
Hebei	78
Gansu	53
Shanxi	30
Ningxia	30
Shaanxi	30
Qinghai	30
Tianjin	41
Beijing	78

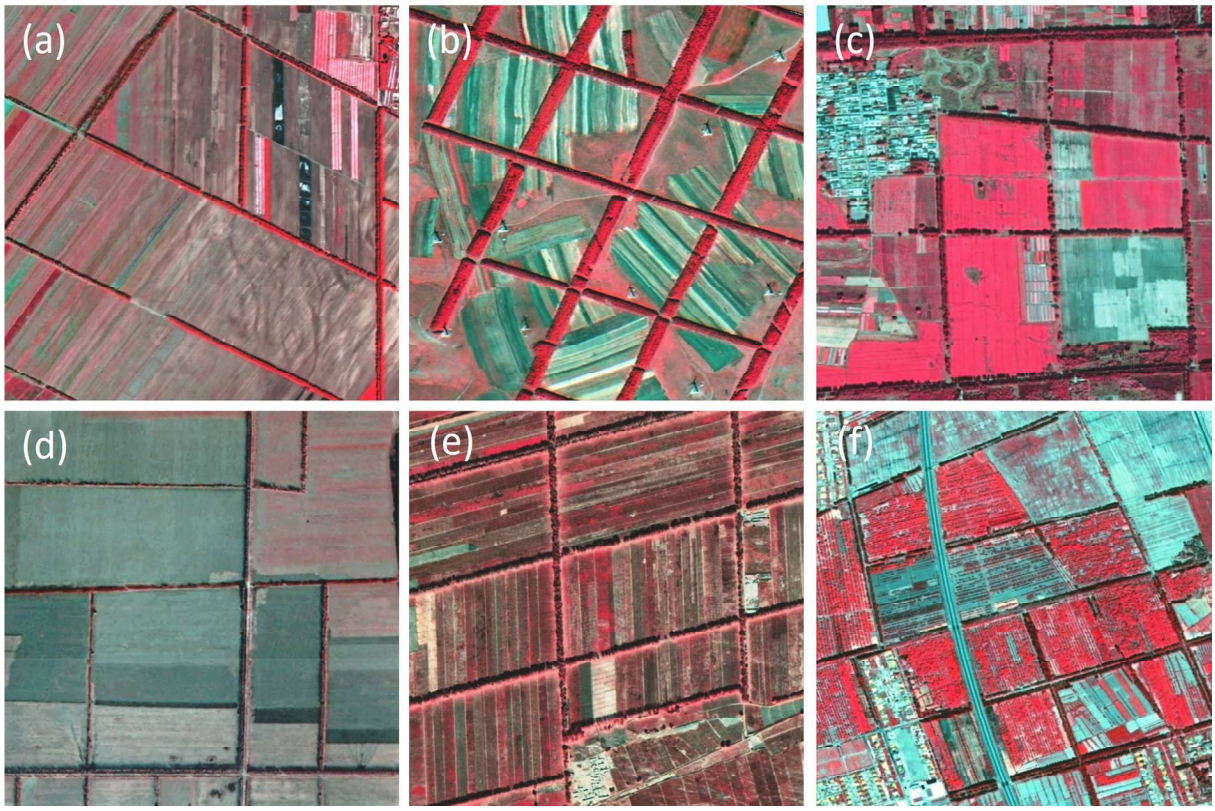


Fig. A2. Examples of GF-1 imagery (2 m resolution, false-colour composite).

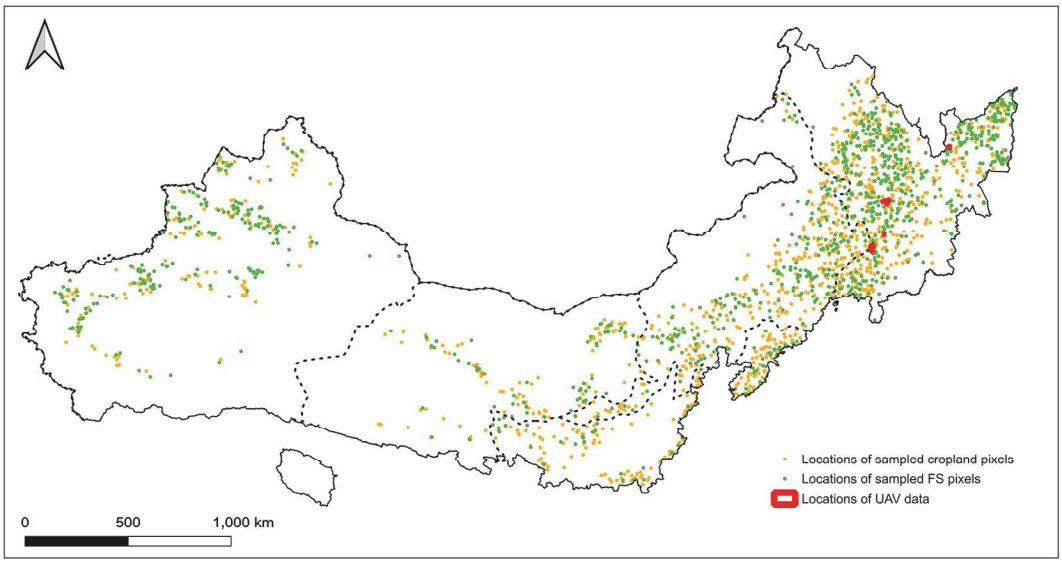


Fig. A3. Spatial distribution of samples (pixels) used for pixel-based accuracy assessment and the locations of UAV data.

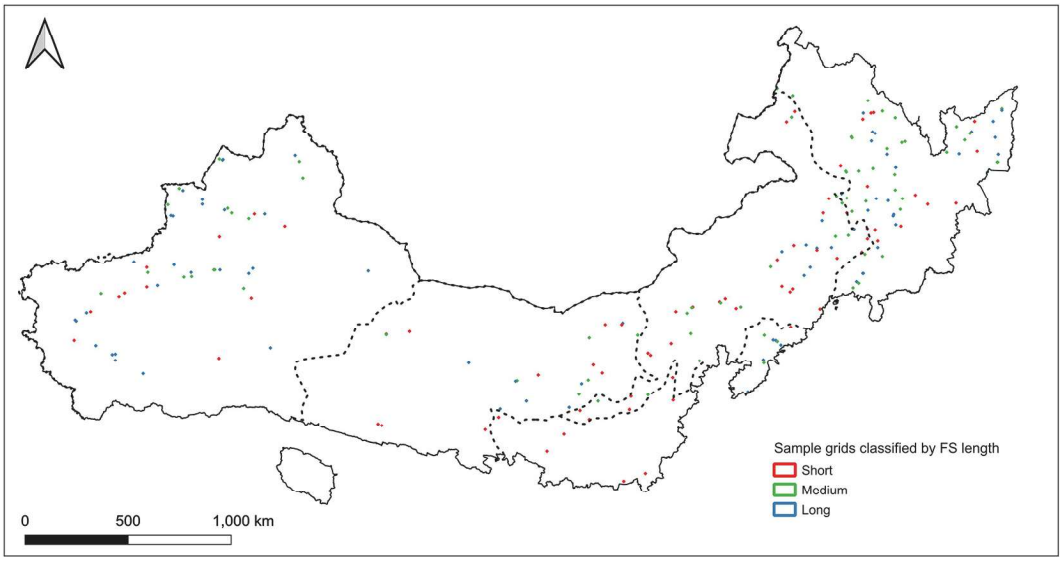


Fig. A4. Spatial distribution of grids used for object-based and length-weighted accuracy assessments.



Fig. A5. UAV imagery and overlay results with FS map.

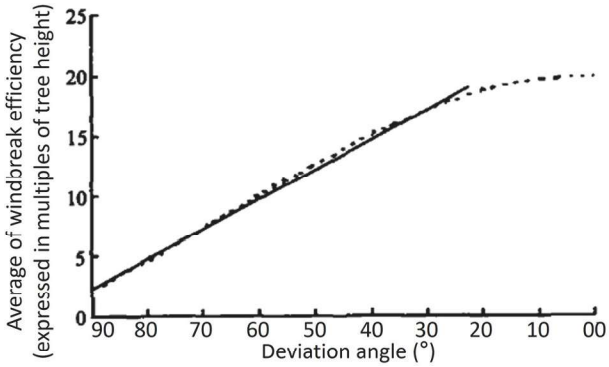


Fig. A6. The relationship between windbreak efficiency and the deviation angle (Zhu, 2023; Zhu et al., 2003).

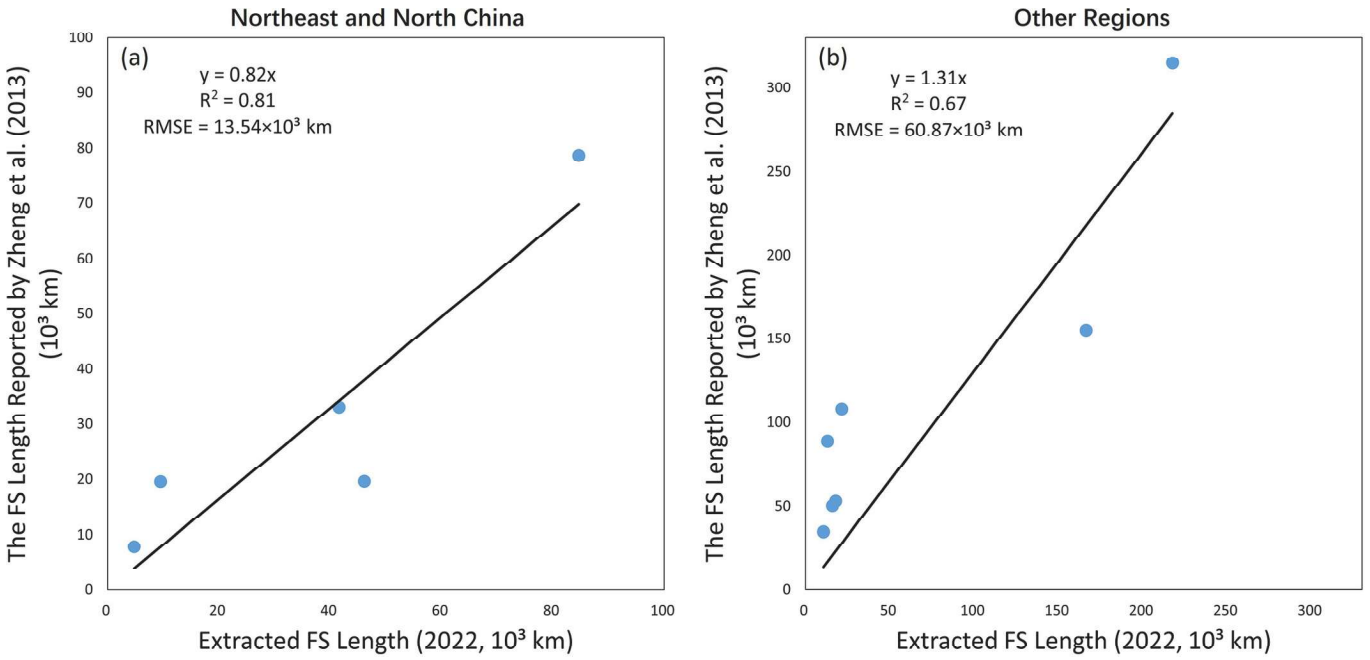


Fig. A7. Comparison between our results and Zheng et al. (2013). (a) in Northeast and North China, where Zheng's estimates were derived from manual visual interpretation. (b) in other regions, where Zheng's estimates were obtained through a sampling-based statistical model relating cropland area to FS length.

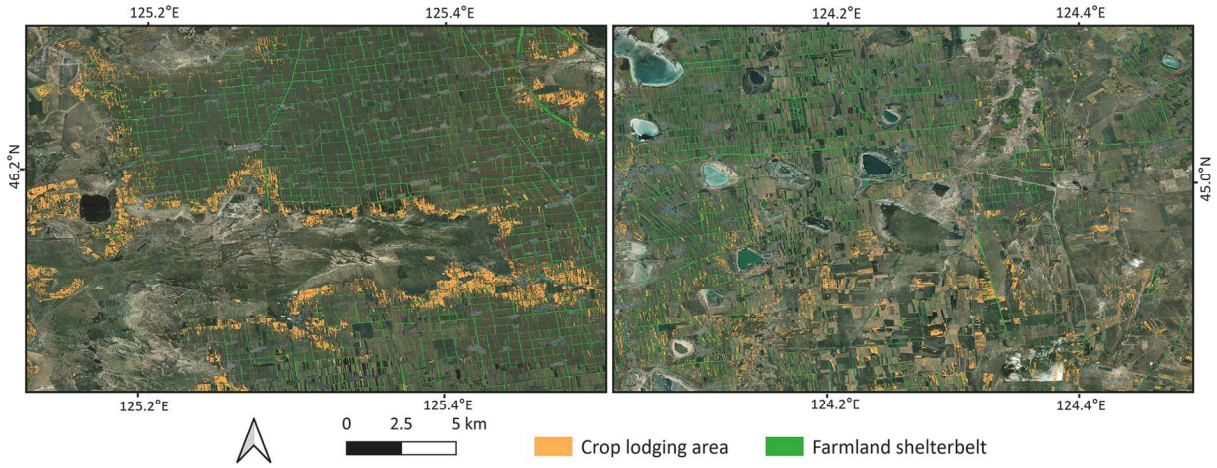


Fig. A8. Examples of the distribution of FSs and lodged crops.

Data availability

The data are available upon request from the authors.

References

Alexey Dosovitskiy, L.B., Kolesnikov, Alexander, Weissenborn, Dirk, Zhai, Xiaohua, Unterthiner, Thomas, Dehghani, Mostafa, Minderer, Matthias, Heigold, Georg, Gelly, Sylvain, Uszkoreit, Jakob, Houlsby, Neil, 2021. An Image is Worth 16x16 Words: Transformers for Image Recognition at Scale, 2021. International Conference on Learning Representations. https://doi.org/10.48550/arXiv.2010.11929.

Baker, T.P., Moroni, M.T., Hunt, M.A., Worledge, D., Mendham, D.S., 2021. Temporal, environmental and spatial changes in the effect of windbreaks on pasture microclimate. Agric. For. Meteorol. 297, 108265. https://doi.org/10.1016/j.agrformet.2020.108265.

Brain, S., 2010. The great Stalin plan for the transformation of nature. Environ. Hist. 15, 670–700. URL. http://www.jstor.org/stable/25764488.

Breiman, L., 2001. Random forests. Mach. Learn. 45, 5–32. https://doi.org/10.1023/A:1010933404324.

Brown, C.F., Brumby, S.P., Guzder-Williams, B., Birch, T., Hyde, S.B., Mazzariello, J., Czerwinski, W., Pasquarella, V.J., Haertel, R., Ilyushchenko, S., Schwehr, K., Weisse, M., Stolle, F., Hanson, C., Guinan, O., Moore, R., Tait, A.M., 2022. Dynamic world, near real-time global 10m land use land cover mapping. Sci Data 9, 251. https://doi.org/10.1038/s41597-022-01307-4.

Cai, X., Henderson, M., Wang, L., Su, Y., Liu, B., 2021. Shelterbelt structure and crop protection from increased typhoon activity in Northeast China. Agriculture 11, 995. https://doi.org/10.3390/agriculture11100995.

Cao, H., Wang, Y., Chen, J., Jiang, D., Zhang, X., Tian, Q., Wang, M., 2022. Swin-unet: Unet-like pure transformer for medical image segmentation. In: European Conference on Computer Vision. Springer, pp. 205–218. https://doi.org/10.48550/arXiv.2105.05537.

Carneiro, T., NóBrega, R.V.M.D., Nepomuceno, T., Bian, G.B., Albuquerque, V.H.C.D., Filho, P.P.R., 2018. Performance analysis of Google Colaboratory as a tool for accelerating deep learning applications. IEEE Access 6, 61677–61685. https://doi.org/10.1109/ACCESS.2018.2874767.

Chang, X., Sun, L., Yu, X., Jia, G., Liu, J., Liu, Z., Zhu, X., Wang, Y., 2019. Effect of windbreaks on particle concentrations from agricultural fields under a variety of wind conditions in the farming-pastoral ecotone of northern China. Agric. Ecosyst. Environ. 281, 16–24. https://doi.org/10.1016/j.agee.2019.04.017.

Chen, J., Cao, X., Peng, S., Ren, H., 2017. Analysis and applications of GlobeLand30: A review. ISPRS Int. J. Geo Inf. 6, 230. https://doi.org/10.3390/ijgi6080230.

Chen, J., Lu, Y., Yu, Q., Luo, X., Adeli, E., Wang, Y., Lu, L., Yuille, A.L., Zhou, Y., 2021. TransUNet: Transformers Make Strong Encoders for Medical Image Segmentation. ArXiv, abs/2102.04306. https://doi.org/10.48550/arXiv.2102.04306.

Chen, Y., Zhou, J., Ge, Y., Dong, J., 2024. Uncovering the rapid expansion of photovoltaic power plants in China from 2010 to 2022 using satellite data and deep learning. Remote Sens. Environ. 305, 114100. https://doi.org/10.1016/j.rse.2024.114100.

Cleugh, H.A., 2002. Field measurements of windbreak effects on airflow, turbulent exchanges and microclimates. Aust. J. Exp. Agric. 42, 665–677. https://doi.org/10.1071/EA02004.

Cochran, W.G., 1977. Sampling techniques. John Wiley & Sons.

Douglas, D.H., Peucker, T.K., 1973. ALGORITHMS for the reduction of the number of points required to represent A digitized line or its caricature. Cartographica 10, 112–122. https://doi.org/10.3138/fm57-6770-u75u-7727.

Forman, R.T., 1995. Land Mosaics: The Ecology of Landscapes and Regions. In:. Cambridge University Press. https://doi.org/10.5822/978-1-61091-491-8_21.

Gao, F., Lv, K., Jiang, Q.O., Xiao, H., Li, J., 2025. How did the regional water-heat distribution in oasis area vary with the different spatial patterns and structures of shelterbelt system—A case study in Ulan Buh desert oasis. Agric. For. Meteorol. 362, 110345. https://doi.org/10.1016/j.agrformet.2024.110345.

Gommes, R., Wu, B., Li, Z., Zeng, H., 2015. Design and characterization of spatial units for monitoring global impacts of environmental factors on major crops and food security. Food Energy Secur. 5, 40–55. https://doi.org/10.1002/fes3.73.

Gong, P., Liu, H., Zhang, M., Li, C., Wang, J., Huang, H., Clinton, N., Ji, L., Li, W., Bai, Y., Chen, B., Xu, B., Zhu, Z., Yuan, C., Ping Suen, H., Guo, J., Xu, N., Li, W., Zhao, Y., Yang, J., Yu, C., Wang, X., Fu, H., Yu, L., Dronova, I., Hui, F., Cheng, X., Shi, X., Xiao, F., Liu, Q., Song, L., 2019. Stable classification with limited sample: transferring a 30-m resolution sample set collected in 2015 to mapping 10-m resolution global land cover in 2017. Sci. Bull. 64, 370–373. https://doi.org/10.1016/j.scib.2019.03.002.

Grace, J., 1988. 3. Plant response to wind. Agric. Ecosyst. Environ. 22-23, 71–88. https://doi.org/10.1016/0167-8809(88)90008-4.

Guo, Y., Wang, Y., Zhao, C., Liu, M., Zhang, X., Shen, Y., 2025. Modelling the impact of agriculture expansion on water scarcity in Xinjiang, China. Ecol. Indic. 177, 113779. https://doi.org/10.1016/j.ecolind.2025.113779.

Heisler, G.M., Dewalle, D.R., 1988. 2. Effects of windbreak structure on wind flow. Agric. Ecosyst. Environ. 22-23, 41–69. https://doi.org/10.1016/0167-8809(88)90007-2.

Khan, A., Rauf, Z., Sohail, A., Khan, A.R., Asif, H., Asif, A., Farooq, U., 2023. A survey of the vision transformers and their CNN-transformer based variants. Artif. Intell. Rev. 56, 2917–2970. https://doi.org/10.1007/s10462-023-10595-0.

Kort, J., 1988. 9. Benefits of windbreaks to field and forage crops. Agric. Ecosyst. Environ. 22-23, 165–190. https://doi.org/10.1016/0167-8809(88)90017-5.

Lechner, A.M., Stein, A., Jones, S.D., Ferwerda, J.G., 2009. Remote sensing of small and linear features: quantifying the effects of patch size and length, grid position and detectability on land cover mapping. Remote Sens. Environ. 113, 2194–2204. https://doi.org/10.1016/j.rse.2009.06.002.

Lei, Z., Lei, T.L., 2024. Large-scale integration of remotely sensed and GIS road networks: A full image-vector conflation approach based on optimization and deep learning. Comput. Environ. Urban. Syst. 113, 102174. https://doi.org/10.1016/j.compenvurbsys.2024.102174.

Lei, S., Sun, H., Liu, H., Jiang, F., Chen, S., Wu, T., Xie, Y., 2020. Study on extraction method of farmland shelterbelt supported by Landsat 8 time series image. J. Cent. South Univ. For. Technol. 40, 57–63. https://doi.org/10.14067/j.cnki.1673-923x.2020.04.009.

Li, B., Sherman, D.J., 2015. Aerodynamics and morphodynamics of sand fences: A review. Aeolian Res. 17, 33–48. https://doi.org/10.1016/j.aeolia.2014.11.005.

Li, C., Guan, W., Fan, X., Zhao, T., Chen, J., Sun, B., 2003. Assessment of landscape ecology of agricultural protection forest system at Beizang town, Daxing County, Beijing. J. For. Res. 14, 135–140. https://doi.org/10.1007/BF02856780.

Li, M., Liu, A., Zou, C., Xu, W., Shimizu, H., Wang, K., 2012. An overview of the "three-north" shelterbelt project in China. For. Stud. China 14, 70–79. https://doi.org/10.1007/s11632-012-0108-3.

Li, X., Liu, L., Xie, J., Wang, Z., Yang, S., Zhang, Z., Qi, S., Li, Y., 2020. Optimizing the quantity and spatial patterns of farmland shelter forests increases cotton productivity in arid lands. Agric. Ecosyst. Environ. 292, 106832. https://doi.org/10.1016/j.agee.2020.106832.

Li, Z., Zhang, H., Lu, F., Xue, R., Yang, G., Zhang, L., 2022. Breaking the resolution barrier: A low-to-high network for large-scale high-resolution land-cover mapping using low-resolution labels. ISPRS J. Photogramm. Remote Sens. 192, 244–267. https://doi.org/10.1016/j.isprsjprs.2022.08.008.

Liu, T., Bao, G., Zhang, D., He, H., Luo, Y., Zhang, Z., 2018. Research on rapid extraction of shelter Forest using GF-2 images based on vegetation indices. For. Eng. 0, 13–19. URL. https://slgc.nefu.edu.cn/EN/Y2018/V0/I6/13.

Liu, R., Ling, J., Zhang, H., 2024. SoftFormer: SAR-optical fusion transformer for urban land use and land cover classification. ISPRS J. Photogramm. Remote Sens. 218, 277–293. https://doi.org/10.1016/j.isprsjprs.2024.09.012.

Lv, W., Zhao, W., 2023. The structure and pattern of farmland shelterbelts in Jiuquan oasis of Hexi corridor. J. Desert Res. 43, 237–245. URL https://www.geores.com.cn/zgsm/EN/10.7522/j.issn.1000-694X.2023.00095.

Ma, Y., Liu, B., Zhang, M., Dong, L., Zhang, G., 2024. Basic characteristics of windbreak in the black soil region of Northeast China and its relationship with wind direction. J. Soil Water Conserv. 38, 207–215. https://doi.org/10.13870/j.cnki.stbcxb.2024.03.001.

McNaughton, K.G., 1988. 1. Effects of windbreaks on turbulent transport and microclimate. Agric. Ecosyst. Environ. 22-23, 17–39. https://doi.org/10.1016/0167-8809(88)90006-0.

Ministry of Agriculture and Rural Affairs of the People's Republic of China, 2022. Well-facilitated farmland construction—General rules.. GB/T 30600–2022 Beijing: State Administration for Market Regulation and State Administration for Market Regulation.

Muro, J., Blickensdörfer, L., Don, A., Köber, A., Asam, S., Schwieder, M., Erasmi, S., 2025. Hedgerow mapping with high resolution satellite imagery to support policy initiatives at national level. Remote Sens. Environ. 328, 114870. https://doi.org/10.1016/j.rse.2025.114870.

Nakahama, N., Hayamizu, M., Iwasaki, K., Nitta, N., 2022. Management and landscape of shelterbelts contribute to butterfly and flowering plant diversity in northern Japan. Ecol. Res. 37, 780–790. https://doi.org/10.1111/1440-1703.12342.

National Forestry and Grassland Administration, 1978. Construction of the Three-North Shelterbelt System: Phase I Project Plan. National Forestry and Grassland Administration Science Data Center. URL. https://www.forestdata.cn/threenorth/.

National Forestry and Grassland Administration, 1986. Construction of the Three-North Shelterbelt System: Phase II Project Plan. National Forestry and Grassland Administration Science Data Center. URL. https://www.forestdata.cn/threenorth/.

National Forestry and Grassland Administration, 1996. Construction of the Three-North Shelterbelt System: Phase III Project Plan. National Forestry and Grassland Administration Science Data Center. URL. https://www.forestdata.cn/threenorth/.

National Forestry and Grassland Administration, 2001. Construction of the Three-North Shelterbelt System: Phase IV Project Plan. National Forestry and Grassland Administration Science Data Center. URL. https://www.forestdata.cn/threenorth/.

National Forestry and Grassland Administration, 2011. Construction of the Three-North Shelterbelt System: Phase V Project Plan. National Forestry and Grassland Administration Science Data Center. URL. https://www.forestdata.cn/threenorth/.

National Forestry and Grassland Administration, 2013. Code for design of farmland shelterbelts engineering. In: *GB/T 50817–2013*. Beijing: China Planning Press.

National Forestry and Grassland Administration, 2019. Construction of the Three-North Shelterbelt System: 40 Years Development Report. National Forestry and Grassland Administration Science Data Center. URL. https://www.forestdata.cn/threenorth/.

Olofsson, P., Foody, G.M., Herold, M., Stehman, S.V., Woodcock, C.E., Wulder, M.A., 2014. Good practices for estimating area and assessing accuracy of land change. Remote Sens. Environ. 148, 42–57. https://doi.org/10.1016/j.rse.2014.02.015.

Orth, J., 2007. The shelterbelt project: cooperative conservation in 1930s America. Agric. Hist. 81, 333–357. URL. http://www.jstor.org/stable/20454725.

Qin, H., Zhou, D., Xu, T., Bian, Z., Li, J., 2025. Factorization vision transformer: modeling long-range dependency with local window cost. IEEE Trans. Neural Networks Learn. Syst. 36, 3151–3164. https://doi.org/10.1109/TNNLS.2023.3342172.

Riitters, K., 2019. Pattern metrics for a transdisciplinary landscape ecology. Landsc. Ecol. 34, 2057–2063. https://doi.org/10.1007/s10980-018-0755-4.

Ronneberger, O., Fischer, P., Brox, T., 2015. U-net: Convolutional networks for biomedical image segmentation. In: Navab, N., Hornegger, J., Wells, W.M., Frangi, A.F. (Eds.), Medical Image Computing and Computer-Assisted Intervention – MICCAI 2015. Springer International Publishing, Cham, pp. 234–241. https://doi.org/10.1007/978-3-319-24574-4_28.

Selvaraju, R.R., Cogswell, M., Das, A., Vedantam, R., Parikh, D., Batra, D., 2020. Grad-CAM: visual explanations from deep networks via gradient-based localization. Int. J. Comput. Vis. 128, 336–359. https://doi.org/10.1007/s11263-019-01228-7.

Shi, X., Li, Y., Deng, R., 2011. A method for spatial heterogeneity evaluation on landscape pattern of farmland shelterbelt networks: A case study in Midwest of Jilin Province, China. Chin. Geogr. Sci. 21, 48–56. https://doi.org/10.1007/s11769-011-0440-x.

Skakun, S., 2025. The impact of map accuracy on area estimation with remotely sensed data within the stratified random sampling design. Remote Sens. Environ. 326, 114805. https://doi.org/10.1016/j.rse.2025.114805.

Sun, Q., Zheng, B., Liu, T., Zhu, L., Hao, X., Han, Z., 2022. The optimal spacing interval between principal shelterbelts of the farm-shelter forest network. Environ. Sci. Pollut. Res. 29, 12680–12693. https://doi.org/10.1007/s11356-021-17272-1.

Takahashi, S., Sakaguchi, Y., Kouno, N., Takasawa, K., Ishizu, K., Akagi, Y., Aoyama, R., Teraya, N., Bolatkan, A., Shinkai, N., Machino, H., Kobayashi, K., Asada, K., Komatsu, M., Kaneko, S., Sugiyama, M., Hamamoto, R., 2024. Comparison of vision transformers and convolutional neural networks in medical image analysis: A systematic review. J. Med. Syst. 48, 84. https://doi.org/10.1007/s10916-024-02105-8.

Teixeira, I., Morais, R., Sousa, J.J., Cunha, A., 2023. Deep learning models for the classification of crops in aerial imagery: A review. Agriculture 13, 965. https://doi.org/10.3390/agriculture13050965.

Tian, F., Wu, B., Zeng, H., Zhang, X., Xu, J., 2019. Efficient identification of corn cultivation area with multitemporal synthetic aperture radar and optical images in the Google earth engine cloud platform. Remote Sens 11, 629. https://doi.org/10.3390/rs11060629.

Wadoux, A.M.J.-C., Heuvelink, G.B.M., 2023. Uncertainty of spatial averages and totals of natural resource maps. Methods Ecol. Evol. 14, 1320–1332. https://doi.org/10.1111/2041-210X.14106.

Wang, Y., Seo, J., Jeon, T., 2022. NL-LinkNet: toward lighter but more accurate road extraction with nonlocal operations. IEEE Geosci. Remote Sens. Lett. 19, 1–5. https://doi.org/10.1109/LGRS.2021.3050477.

Wang, J., Patruno, L., Zhao, G., Tamura, Y., 2024. Windbreak effectiveness of shelterbelts with different characteristic parameters and arrangements by means of CFD simulation. Agric. For. Meteorol. 344, 109813. https://doi.org/10.1016/j.agrformet.2023.109813.

Wu, B., 2017. China's Land Cover. Beijing: China Science Publishing & Media Ltd. (CSPM).

Wu, B., Gommes, R., Zhang, M., Zeng, H., Yan, N., Zou, W., Zheng, Y., Zhang, N., Chang, S., Xing, Q., Van Heijden, A., 2015. Global crop monitoring: A satellite-based hierarchical approach. Remote Sens 7, 3907–3933. https://doi.org/10.3390/rs70403907.

Wu, B., Fu, Z., Fu, B., Yan, C., Zeng, H., Zhao, W., 2024. Dynamics of land cover changes and driving forces in China's drylands since the 1970 s. Land Use Policy 140, 107097. https://doi.org/10.1016/j.landusepol.2024.107097.

Xie, E., Wang, W., Yu, Z., Anandkumar, A., Alvarez, J.M., Luo, P., 2021. SegFormer: simple and efficient design for semantic segmentation with transformers. In: NIPS'21: Proceedings of the 35th International Conference on Neural Information Processing Systems, pp. 12077–12090. https://doi.org/10.48550/arXiv.2105.15203.

Xu, Z., Liu, Y., Gan, L., Sun, Y., Wu, X., Liu, M., Wang, L., 2022. RNGDet: road network graph detection by transformer in aerial images. IEEE Trans. Geosci. Remote Sens. 60, 1–12. https://doi.org/10.1109/TGRS.2022.3186993.

Yao, J., Zhang, B., Li, C., Hong, D., Chanussot, J., 2023. Extended vision transformer (ExViT) for land use and land cover classification: A multimodal deep learning framework. IEEE Trans. Geosci. Remote Sens. 61, 1–15. https://doi.org/10.1109/TGRS.2023.3284671.

Zanaga, D., Van De Kerchove, R., Daems, D., De Keersmaecker, W., Brockmann, C., Kirches, G., Wevers, J., Cartus, O., Santoro, M., Fritz, S., Lesiv, M., Herold, M., Tsendbazar, N.E., Xu, P., Ramoino, F., Arino, O., 2022. ESA WorldCover 10 m 2021 v200. https://doi.org/10.5281/zenodo.7254221.

Zhai, J., Wang, L., Liu, Y., Wang, C., Mao, X., 2023. Assessing the effects of China's three-north shelter Forest program over 40 years. Sci. Total Environ. 857, 159354. https://doi.org/10.1016/j.scitotenv.2022.159354.

Zhang, T.Y., Suen, C.Y., 1984. A fast parallel algorithm for thinning digital patterns. Commun. ACM 27, 236–239. https://doi.org/10.1145/357994.358023.

Zhang, X., Liu, L., Chen, X., Gao, Y., Xie, S., Mi, J., 2021. GLC_FCS30: global land-cover product with fine classification system at 30 m using time-series Landsat imagery. Earth Syst. Sci. Data 13, 2753–2776. https://doi.org/10.5194/essd-13-2753-2021.

Zhao, Q., Jiang, P., Wang, X., Zhang, L., Zhang, J., 2021. Classification of protection Forest tree species based on UAV hyperspectral data. Trans. Chin. Soc.Agric. Mach 52, 190–199. https://doi.org/10.6041/j.issn.1000-1298.2021.11.020.

Zheng, X., Zhu, J., 2015a. A methodological approach for spatial downscaling of TRMM precipitation data in North China. Int. J. Remote Sens. 36, 144–169. https://doi.org/10.1080/01431161.2014.995275.

Zheng, X., Zhu, J., 2015b. Temperature-based approaches for estimating monthly reference evapotranspiration based on MODIS data over North China. Theor. Appl. Climatol. 121, 695–711. https://doi.org/10.1007/s00704-014-1269-x.

Zheng, X., Zhu, J., Yan, Y., 2013. Estimation of farmland shelterbelt area in the three-north shelter/protective Forest program regions of China based on multi-scale remote sensing data. China. J. Ecol. 32, 1355–1363. URL. https://www.cje.net.cn/EN/Y2013/V32/I5/1355.

Zheng, X., Zhu, J., Xing, Z., 2016. Assessment of the effects of shelterbelts on crop yields at the regional scale in Northeast China. Agric. Syst. 143, 49–60. https://doi.org/10.1016/j.agsy.2015.12.008.

Zheng, X., Zhu, J., Wang, G.G., Yan, Q., Sun, T., Song, L., Gao, T., Sun, Y., Li, X., Yang, K., Zhang, J., Yu, L., Qi, K., Zhao, L., Lu, D., Lu, Z., 2025. Assessing the ecological effects of the World's largest forestry eco-engineering: three-north protective Forest program within the initially scheduled range from 1978 to 2022. Sci. China Life Sci. 68, 314–327. https://doi.org/10.1007/s11427-024-2705-4.

Zhou, X., Sun, Z., 1994. ON MEASURING AND EVALUATING THE SPATIAL PATTERN OF SHELTERBELT TNETWORKS IN LANDSCAPE. Acta Ecol. Sin. 14, 24–31. URL https://www.ecologica.cn/stxb/article/abstract/940104?st=search.

Zhou, D., Yu, Z., Xie, E., Xiao, C., Anandkumar, A., Feng, J., Alvarez, J.M., 2022. Understanding the robustness in vision transformers. In: Kamalika, C., Stefanie, J., Le, S., Csaba, S., Gang, N., Sivan, S. (Eds.), Proceedings of the 39th International Conference on Machine Learning. Proceedings of Machine Learning Research: PMLR, pp. 27378–27394. URL. https://proceedings.mlr.press/v162/zhou22m.html.

Zhu, J., 2023. Ecology of Protective Forests. Beijing: China Science Publishing & Media Ltd. (CSPM).

Zhu, J., Zheng, X., 2019. The prospects of development of the three-north afforestation program (TNAP): on the basis of the results of the 40-year construction general assessment of the TNAP. China. J. Ecol. 38, 1600–1610. URL. https://www.cje.net.cn/EN/Y2019/V38/I5/1600.

Zhu, J., Jiang, F., Zhiping, F., Zhou, X., 2003. Optimization of spatial arrangements and patterns for shelterbelts or windbreaks. Chin. J. Appl. Ecol. 1205–1212. URL. https://qikan.cqvip.com/Qikan/Article/Detail?id=8278562.

Zhu, J., He, K., Wei, T., 2010. Science of Farmland Shelterbelt. Beijing: China Forestry Publishing House.